CELL BIOLOGY

Nebulin and Lmod2 are critical for specifying thin-filament length in skeletal muscle

Balázs Kiss[1]*, Jochen Gohlke[1], Paola Tonino[1], Zaynab Hourani[1], Justin Kolb[1], Joshua Strom[1], Olga Alekhina[1], John E. Smith III[1], Coen Ottenheijm[1], Carol Gregorio[1], Henk Granzier[1,2]†

Regulating the thin-filament length in muscle is crucial for controlling the number of myosin motors that generate power. The giant protein nebulin forms a long slender filament that associates along the length of the thin filament in skeletal muscle with functions that remain largely obscure. Here nebulin's role in thin-filament length regulation was investigated by targeting entire super-repeats in the *Neb* gene; nebulin was either shortened or lengthened by 115 nm. Its effect on thin-filament length was studied using high-resolution structural and functional techniques. Results revealed that thin-filament length is strictly regulated by the length of nebulin in fast muscles. Nebulin's control is less tight in slow muscle types where a distal nebulin-free thin-filament segment exists, the length of which was found to be regulated by leiomodin-2 (Lmod2). We propose that strict length control by nebulin promotes high-speed shortening and that dual-regulation by nebulin/Lmod2 enhances contraction efficiency.

INTRODUCTION

The thin filament is an essential component of the sarcomere (contractile unit of muscle) where it anchors in the Z-disk (barbed-end), extends toward the middle of the sarcomere (pointed-end), and overlaps with myosin-containing thick filaments. How thin-filament length (TFL) is controlled needs to be well understood as TFL dysregulation is known to occur in various myopathies (*1*–*3*). In skeletal muscle, the thin filament comprises filamentous actin (F-actin), regulatory proteins (*4*), capping proteins (*2*) and, importantly, nebulin (*5*). Nebulin is a giant molecule that forms a long slender filament that coextends with F-actin, from its barbed-end to close to its pointed-end (*6*). An early ground-breaking study revealed a positive correlation between the TFL and the length of nebulin (*7*), giving rise to the proposal that nebulin is a "molecular ruler." This hypothesis is consistent with the structure of nebulin that contains small actin-binding motifs clustered into seven-motif–containing super-repeats (25 in the mouse, S1 to S25), each of which is likely to span an F-actin helical repeat unit (*8*, *9*).

Although the ruler hypothesis is attractive, subsequent studies proposed that instead of nebulin, pointed-end interacting proteins regulate TFL with complex roles played by tropomodulin isoforms (Tmod1 and Tmod2) that shorten and leiomodin isoforms (Lmod2 and Lmod3) that lengthen the thin filament [for a review, see (*2*)]. Lmod2 has recently been shown to lengthen the thin filament in cardiac muscle, where nebulin is absent, and it is thought that in skeletal muscle, Lmod3 plays a similar role (*10*–*14*).

To critically study the role of nebulin in TFL regulation, we created two mouse models: one with nebulin super-repeats S9, S10, and S11 deleted (Neb$^{\Delta S9-11}$) and another in which these super-repeats are duplicated (Neb$^{DupS9-11}$), producing a smaller and a super-sized nebulin, respectively. These genetic models are ideal for critically examining the role of nebulin in TFL regulation in skeletal muscle. The lengths of nebulin and the thin filament were studied in various peripheral and diaphragm muscles using super-resolution structured illumination microscopy (SR-SIM), immunoelectron microscopy (IEM), transcriptomics, and biophysical techniques. Pointed-end binding proteins (Lmod2/3 and Tmod1/4) were also studied to determine their possible role in antagonizing or augmenting nebulin-based changes in TFL. Results revealed that nebulin functions as a molecular ruler for thin filaments in fast-contracting muscle and that in slow muscles nebulin's ruler function is augmented at the thin-filament pointed-end by Lmod2. This study provides unexpected insights in TFL regulation in skeletal muscle and, as discussed in detail below, has clinical implications for both skeletal and cardiac muscle diseases.

RESULTS

Successful creation of mouse models expressing shortened and lengthened nebulin

The two models that were created, one in which super-repeats S9 to 11 are deleted, the Neb$^{\Delta S9-11}$ model, and the other in which super-repeats S9 to 11 are duplicated, the Neb$^{DupS9-11}$ model, are explained in Fig. 1A with technical details in Materials and Methods. For each model, offspring of Het × Het breeder pairs were born at Mendelian ratios (fig. S1A) and had normal body weights (fig. S1B). Furthermore, skeletal muscles of Hom Neb$^{\Delta S9-11}$ and Hom Neb$^{DupS9-11}$ mice exhibited identical weights and myosin isoform expression patterns when compared to wild-type (WT) littermates (fig. S1, C to E). Protein gels showed that nebulin in Neb$^{\Delta S9-11}$ mice had increased mobility and in Neb$^{DupS9-11}$ mice reduced mobility, as expected, and that total nebulin protein levels were not different from WT levels (Fig. 1B). Crossing Neb$^{\Delta S9-11}$ and Neb$^{DupS9-11}$ mice resulted in Neb$^{\Delta S9-11/DupS9-11}$ mice, referred to as compound-Het mice, which were also viable and developed normally (fig. S2). Their muscles expressed two nebulin isoforms, with a combined expression level similar to that of WT littermates (Fig. 1C). IEM on extensor digitorum longus (EDL) muscles from Hom Neb$^{\Delta S9-11}$ and Hom Neb$^{DupS9-11}$ mice labeled with an antibody to nebulin's N terminus showed that both mutant nebulins assemble normally into the sarcomere with no obvious changes in

---

[1] Department of Cellular and Molecular Medicine, University of Arizona, Tucson, AZ 85721, USA. [2] Allan and Alfie Endowed Chair for Heart Disease in Women Research, Sarver Molecular Cardiovascular Research Program, University of Arizona, Tucson, AZ 85721, USA.
*Present address: Department of Biophysics and Radiation Biology, Semmelweis University, 1094 Budapest, Hungary.
†Corresponding author. Email: granzier@arizona.edu

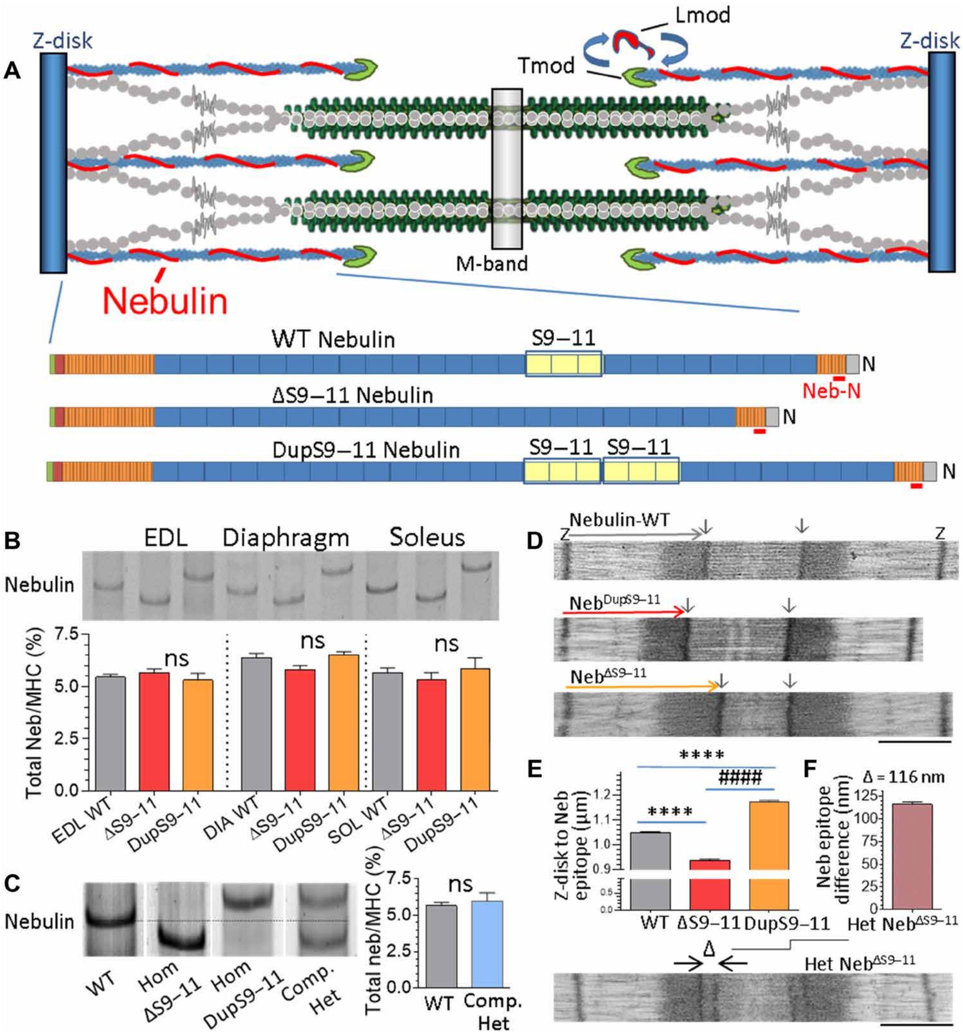

Fig. 1. Basic characterization of mouse models expressing shortened and lengthened nebulin, the Neb$^{\Delta S9-11}$, and Neb$^{DupS9-11}$ models. (**A**) Schematic of skeletal muscle sarcomere. Nebulin's C terminus is anchored in the Z-disk, and its N terminus is near the thin-filament pointed-end (capped by Tmod and interacting with leiomodin Lmod). Nebulin super-repeats 9 to 11 and the antibody against its N-terminal modules are highlighted. In the Neb$^{\Delta S9-11}$ and Neb$^{DupS9-11}$ nebulin models, S9 to 11 have been deleted and duplicated, respectively. (**B**) Nebulin expression in EDL, diaphragm, and soleus muscles of Hom mice, normalized to myosin heavy chain (MHC). Nebulin expression is not altered in the gene targeted mice. (**C**) Nebulin expression in EDL muscle of WT, Hom Neb$^{\Delta S9-11}$, Hom Neb$^{DupS9-11}$, and a compound heterozygous cross of these models (referred to as compound-Het). Dotted line: location of WT nebulin. Total nebulin expression in the compound-Het EDL muscle is the same as in WT muscle. (**D**) IEM with the nebulin N-terminal antibody resulted in clear labeling (arrows) that revealed the sarcomeric incorporation of shorter and longer nebulin, compared to WT, in Hom Neb$^{\Delta S9-11}$ and Hom Neb$^{DupS9-11}$ EDL, respectively. (**E**) Analyzed nebulin length results. (**F**) Results of Het Neb$^{\Delta S9-11}$ EDL labeled by the nebulin N-terminal antibody. A doublet is detected in the sarcomere with 116-nm separation. Scale bars, 500 nm. [Graphs, means ± SEM; (B) and (E), comparisons based on analysis of variance (ANOVA); NS, nonsignificant. ****$P < 0.0001$ in comparison versus WT; ####$P < 0.0001$ in comparison versus Neb$^{\Delta S9-11}$. (C), comparison based on unpaired two-tailed *t* test.].

the overall sarcomere structure (Fig. 1D). The distance between nebulin's N terminus and the middle of the Z-disk was clearly reduced in Neb$^{\Delta S9-11}$ mice and increased in Neb$^{DupS9-11}$ mice compared with WT (Fig. 1E). IEM performed on Het Neb$^{\Delta S9-11}$ EDL sarcomeres showed that they contained two nebulin populations with a 116-nm distance between their N termini (Fig. 1F). Overall, it can be concluded that we successfully created two contrasting mouse models with shortened or lengthened nebulin molecules and that insertion or deletion of nebulin super-repeats was well tolerated as no changes in body weight, muscle weight, fiber-type, and overall sarcomere structure were observed. These new models are unique tools to directly study the role of nebulin in TFL regulation.

Transcript analysis revealed nebulin exon usage and Lmod2 gene expression changes

To establish whether deletion or addition of S9 to 11 had unintended consequences (e.g., aberrant RNA splicing) an RNA sequencing (RNA-seq) study was performed using the EDL, soleus, and diaphragm muscles, selected because of their distinct functions. The expression levels of each of the 166 *Neb* exons in WT, Neb$^{\Delta S9-11}$, and Neb$^{DupS9-11}$ mice, calculated as percent spliced in (PSI), are shown in Fig. 2 and table S1 with *P* values for differences in fig. S3A. In WT mice, the three muscle types had identical and fully expressed exons in nebulin's N terminus (Fig. 2, pink). The 25 super-repeat containing region (exons 14 to 139) was fully expressed in all muscle types

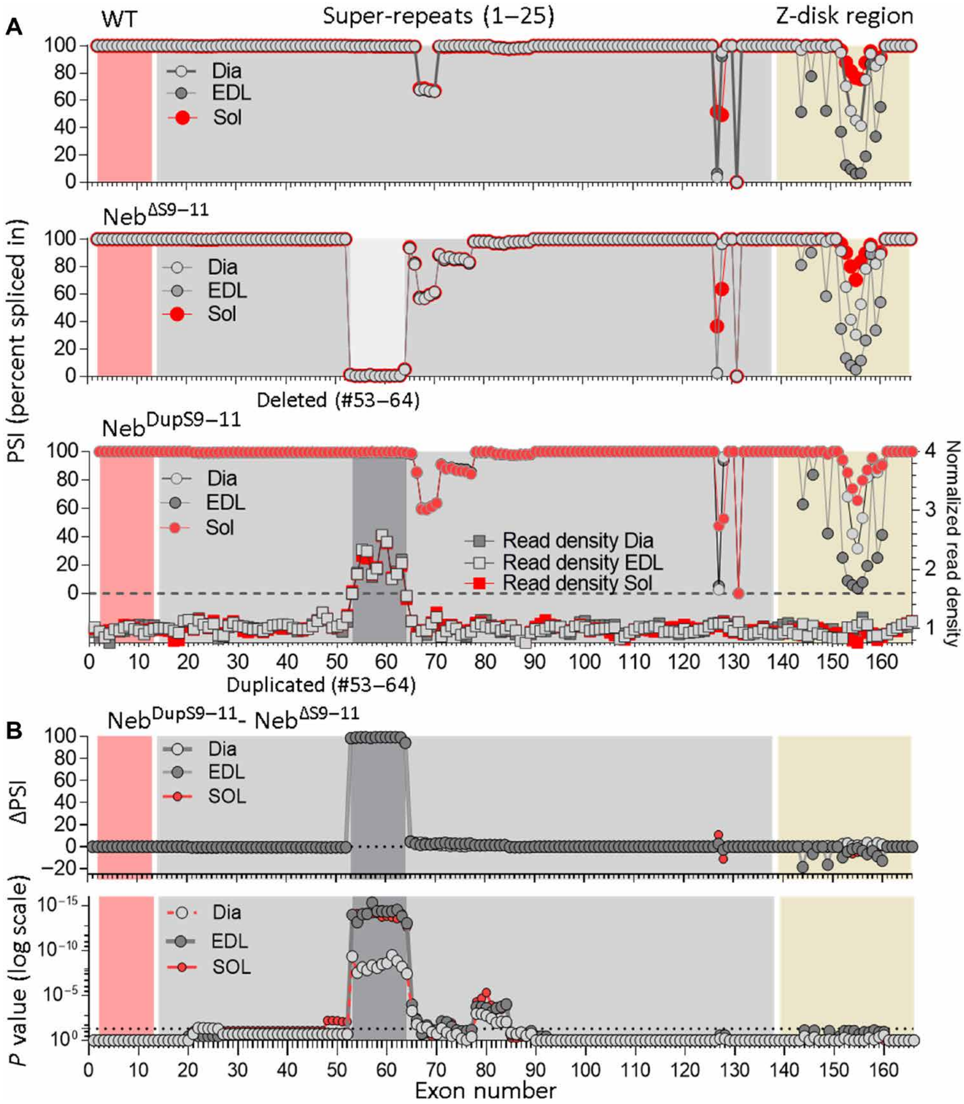

Fig. 2. Nebulin exon expression in WT, Hom Neb$^{\Delta S9-11}$, and Hom Neb$^{DupS9-11}$ mice, shown as PSI. (**A**) Expression analysis in soleus (Sol), EDL, and diaphragm (Dia) muscle in WT (top), Neb$^{\Delta S9-11}$ (middle), and Neb$^{DupS9-11}$ (bottom) mice. Indicated are the various regions of the gene, corresponding to nebulin's N terminus (pink), super-repeat region (gray), and Z-disk region (yellow). Shown are also the targeted exons 53 to 64 that were deleted in the Neb$^{\Delta S9-11}$ (middle) and duplicated in the Neb$^{DupS9-11}$ model (bottom). Because the added exons 53 to 64 cannot be distinguished from the native exons, the normalized read density of exons 53 to 64 were determined (bottom, right scale), revealing a higher read density for exons 53 to 64. Note that in the gene-targeted mice, there are minimal adaptations in PSI outside the targeted region. (**B**) Top: Difference in PSI for Hom Neb$^{\Delta S9-11}$ and Hom Neb$^{DupS9-11}$ exons. Bottom: *P* values for Neb$^{\Delta S9-11}$ - Neb$^{DupS9-11}$ PSI comparison (Shown values are the mean of 12 mice. For additional details, see fig. S3, A to D, and table S1.).

(Fig. 2, gray area) with the following exceptions. Exon 131, which encodes a domain homologous to human tight junction protein ZO-1 (*15*), was not expressed in any of the muscle types. Furthermore, exon 127 was spliced out and exon 128 included in EDL and diaphragm muscles, whereas both exons were equally expressed in soleus muscle. These results are consistent with earlier quantitative polymerase chain reaction (qPCR) studies (*16*). Last, exons 67 to 70 were submaximally expressed: 67 ± 1%, 67 ± 1%, and 68 ± 1% in diaphragm, EDL, and soleus, respectively. Exons 67 to 70 encode seven simple repeats (table S1), equivalent to one super-repeat. Overall, exon expression analysis in the super-repeat region of WT muscles supports the notion that a relatively small fraction of transcripts contains 24 super-repeats and that most of the nebulin transcripts contain 25 super-repeats.

In contrast to the super-repeat region, large differences in exon expression in WT mice were found in the Z-disk exons 152 to 160, with high PSI values in soleus muscle (average 88 ± 7%), low values in EDL (23 ± 17%) and intermediate PSI values in diaphragm (69 ± 21%). (Fig. 3 and figs. S3, B and C). It is known that the Z-disk thickness varies in different muscle types (*17*), in the mouse the Z-disk thickness is ~50 nm in EDL and ~100 nm in soleus muscle (*18*, *19*). Thus, nebulin exon inclusion in the Z-disk positively correlates with Z-disk thickness.

In the S9 to 11 deletion and duplication models, exon expression in the N terminus and the Z-disk region of nebulin showed no differences from WT mice (Figs. 2 and 3 and table S1). In the super-repeat region, exons 53 to 64 were, as expected, absent in the Neb$^{\Delta S9-11}$ model

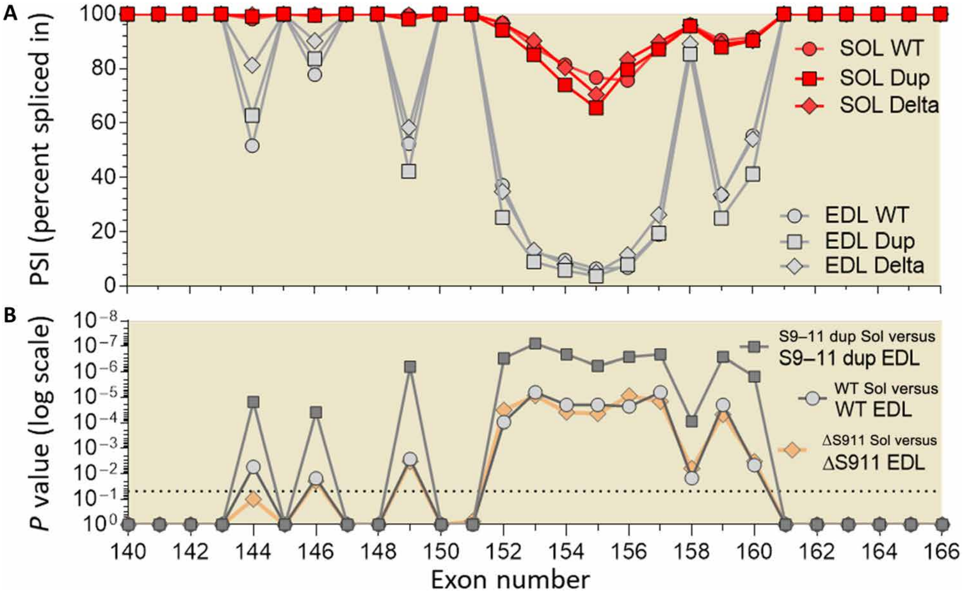

Fig. 3. PSI of Z-disk exons (Neb exons 140 to 166) in soleus and EDL muscle. (**A**) PSI values in WT (circles), Neb$^{\Delta\mathrm{S9-11}}$ (diamond), and Neb$^{\mathrm{DupS9-11}}$ (squares) genotypes. (**B**) *P* values for PSI difference between soleus and EDL in WT (circles), Neb$^{\Delta\mathrm{S9-11}}$ (diamond), and Neb$^{\mathrm{DupS9-11}}$ (squares) genotypes. Exons 152 to 160 expression varies greatly between soleus and EDL muscles, but genotype has little effect.

(Fig. 2). In Neb$^{\mathrm{DupS9-11}}$ mice exons 53 to 64 were duplicated and considering that in WT mice these exons were expressed at 100% and that the PSI per definition cannot exceed 100%, exons 53 to 64 in the Neb$^{\mathrm{DupS9-11}}$ mice also show as 100% expressed (Fig. 2A, bottom panel). As an alternative to PSI, the read density of exons was determined. This established that exons 53 to 64 are at elevated read density in the Neb$^{\mathrm{DupS9-11}}$ mice (Fig. 2A, bottom panel, bottom three traces, right *y* axis), consistent with their duplication.

The exon expression levels outside the targeted region of the Neb$^{\mathrm{DupS9-11}}$ and Neb$^{\Delta\mathrm{S9-11}}$ mice were similar to those in WT mice, with minor exceptions in exons 65 to 78 (fig. S3D). Exon skipping events were analyzed using splice junction reads (see Materials and Methods and table S2). Most frequent was skipping of exons 66 to 71, followed by exons 65 to 78 and exons 69 to 78 (fig. S3D). Exons 67 to 70, which were included in ~70% of transcripts in WT mice, were present at a slightly lower percentage in both Neb$^{\Delta\mathrm{S9-11}}$ and Neb$^{\mathrm{DupS9-11}}$ mice (~60% PSI). Furthermore, exons 71 to 77, which were maximally expressed in WT, were skipped in 10 to 15% of transcripts in both Neb$^{\Delta\mathrm{S9-11}}$ and Neb$^{\mathrm{DupS9-11}}$ mice (fig. S3D). Note that exons were always skipped in intervals of seven nebulin simple repeats, which form one super-repeat unit (seven actin-binding simple repeats, one of which contains a tropomyosin-binding sequence). Thus, expression analysis in the super-repeat region of the *Neb* gene indicates modest reductions in expression levels of a small number of super-repeats. However, the differences in PSI values (ΔPSI) of Neb$^{\mathrm{DupS9-11}}$ and Neb$^{\Delta\mathrm{S9-11}}$ compared to WT mice were small, and ΔPSI between Neb$^{\mathrm{DupS9-11}}$ and Neb$^{\Delta\mathrm{S9-11}}$ mice was zero, except for the targeted region (Fig. 2B). Consequently, when studying structural and functional differences between Neb$^{\mathrm{DupS9-11}}$ and Neb$^{\Delta\mathrm{S9-11}}$ mice, the direct comparison between these two contrasting genotypes will be most powerful as they differ in six super-repeats with negligible differences in exons elsewhere.

The expression levels of all genes are shown in table S3 (tabs 1 to 10). Differentially regulated pathways were studied with a Gene Ontology term analysis, and results are summarized in table S3 (tabs 11 to 19). Overall, only small differences in gene expression levels were found. A comparison between Neb$^{\mathrm{DupS9-11}}$ mice and Neb$^{\Delta\mathrm{S9-11}}$ of multiple differential genes that are involved in anchoring thin filaments in the Z-disk and stabilizing thin filaments is shown in table S3 (tab 20); a comparison of transcript levels for thin-filament pointed-end interacting proteins in Neb$^{\mathrm{DupS9-11}}$ and Neb$^{\Delta\mathrm{S9-11}}$ mice is shown in fig. S4 (A to C). Lmod2 stands out as its expression level was very high, particularly in soleus muscle. A two-way analysis of variance (ANOVA) (with muscle type and genotype as factors) shows that Lmod2 expression was significantly dependent on both genotype and muscle type, with a significantly reduced Lmod2 level in Neb$^{\mathrm{DupS9-11}}$ mice compared to Neb$^{\Delta\mathrm{S9-11}}$ mice (fig. S4D, see also below).

Nebulin length and TFL vary coordinately in EDL muscle

Nebulin length, TFL, and A-band width were measured with SR-SIM on sections of stretched EDL muscle (Fig. 4A), a muscle specialized for fast contractions fueled by glycolysis. A-band width, measured with the Ti102 antibody against A/I junctional titin epitopes (*20*), was close to 1.60 μm in all three genotypes (fig. S5A). Nebulin length was determined from the location of nebulin's N terminus to the middle of the Z-disk with measurements obtained across a broad sarcomere length (SL) range. Nebulin length and other thin filament–related epitope distances have been reported to depend on SL (*21*), and this was confirmed in the present study (Fig. 4B, see also the caption of fig. S5). Most TFL changes took place at relatively short SLs with small changes at SLs beyond ~2.5 μm. In this study, we report average values in the 2.6- to 3.0-μm SL range. The obtained nebulin length in WT EDL was 1028 nm, the N terminus of nebulin localized 107 nm proximal or 121 nm distal from nebulin's WT N terminus in Hom Neb$^{\Delta\mathrm{S9-11}}$ or Neb$^{\mathrm{DupS9-11}}$ EDL, respectively (Fig. 4, B and C).

TFL measured with a Tmod1 antibody (to mark the actin-filament pointed-end) or with fluorescently labeled phalloidin that labels F-actin gave similar results (Fig. 4B). In all three genotypes, the thin

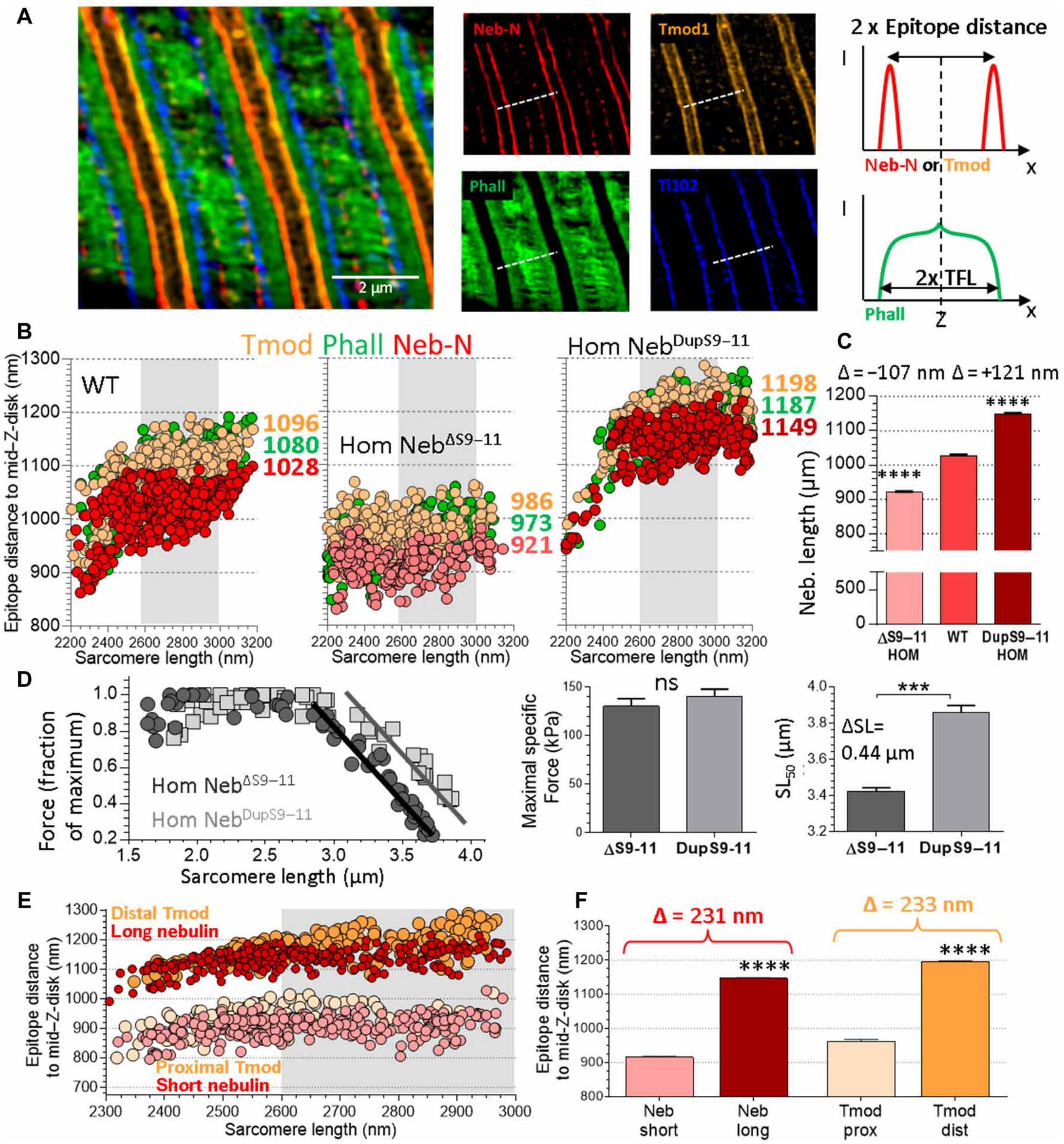

Fig. 4. Nebulin length, thin-filament length, and force-sarcomere length relation in EDL muscle. (**A**) Examples SR-SIM images on skinned Neb$^{DupS9-11}$ Hom EDL muscle. Left: merged, middle: individual channels; red: N terminus of nebulin, orange: Tmod1, green: phalloidin, blue: A-band (Ti102 antibody). Right: Neb-N and Tmod1 epitope distance together with TFL were measured on intensity plot profiles across the Z-disk. (The Ti102 epitope distance was measured across the A-band.). (**B**) SL dependence of the TFL and nebulin epitope to mid–Z-disk distance. The numbers represent the mean results averaged in the 2.6- to 3.0-μm SL range. (**C**) Nebulin length (average ± SEM). The shown length difference at the top is compared to WT. (**D**) Left: F-SL relationship for Hom Neb$^{\Delta S9-11}$ and Neb$^{DupS9-11}$ EDL muscle fibers. The descending limbs of these relationships are offset along the SL axis. (D) Right: Specific force at optimal SL; SL_{50}: SL at half-maximal active force. (**E**) SL dependence of the short and long nebulin isoforms and proximal and distal Tmod epitopes (see also fig. S7A) in EDL muscle of compound Het Neb$^{\Delta S9-11/DupS9-11}$. (**F**) Results in the 2.6- to 3.0-μm SL range [gray in (E)]. [Graphs: means ± SEM. (C) ANOVA. ****$P < 0.0001$ in comparison versus WT. (D, right) and (F): unpaired two-tailed *t* test. ***$P < 0.001$; ****$P < 0.0001$; ns, not significant)]

filaments protruded ~50 nm beyond nebulin (Fig. 4B). Thin filaments of the Hom Neb$^{\Delta S9-11}$ were shortened by ~109 nm compared to WT and lengthened by ~105 nm in the Hom Neb$^{DupS9-11}$ EDL (Fig. 4B), and, thus, TFL appears to follow nebulin length. The correlation between nebulin length and TFL can be assessed from the slope of the TFL-nebulin length relationship, with a theoretical slope of 1.0 indicating that nebulin fully dictates TFL. The experimentally determined slopes were 0.94 and 0.93 for the phalloidin-based and Tmod-based TFL, respectively (a side-by-side comparison with other muscle types is given below). These slopes were not significantly different from 1.0, revealing nebulin's important role in TFL specification in EDL muscle.

IEM with the nebulin N-terminal antibody was also used to establish the nebulin length by measuring the distance between the middle of the Z-disk and the antibody epitope in immuno-labeled sarcomeres; TFL was measured between the middle of the Z-disk and the H-zone on unlabeled micrographs (Fig. 5, A and B). Nebulin and thin filaments were 237 and 240 nm shorter, respectively, in Neb$^{\Delta S9-11}$ compared to Neb$^{DupS9-11}$ (Fig. 5, C and D). Also, these data support that in EDL muscle, TFL closely follows the length of nebulin.

To determine how the altered TFLs affect muscle function, the descending limb of the force-SL (F-SL) relation was measured. Studies were performed on skinned EDL fiber bundles that were stretched to a given SL and then activated by a maximal level of activating calcium. Once force had reached a maximal level, the muscle was relaxed again, and the protocol was repeated at a different SL. The measured forces were divided by the maximal force at the optimal SL and normalized F-SL curves were thus obtained. Results revealed a 440-nm displacement of the descending limb in Neb$^{\Delta S9-11}$ relative to Neb$^{DupS9-11}$ (Fig. 4D) or 220 nm per half sarcomere. This value is in agreement with the measured difference in TFL [228 nm (Tmod), 214 nm (phalloidin), and 240 nm (EM)]. At a given length on the descending limb of the F-SL relation the Neb$^{\Delta S9-11}$ muscle fibers generated much lower forces than Neb$^{DupS9-11}$ fibers.

We also studied the EDL muscle in compound-Het mice (Neb$^{\Delta S9-11/DupS9-11}$) mice obtained by breeding Neb$^{\Delta S9-11}$ and Neb$^{DupS9-11}$ mice. The two nebulin isoforms were incorporated into the sarcomeres as indicated by the two N-terminal nebulin epitopes per half sarcomere (fig. S6A). The average length of the two isoforms (short, 916 nm; long, 1147 nm; Fig. 4, E and F) is in agreement with the Hom Neb$^{\Delta S9-11}$ and the Hom Neb$^{DupS9-11}$ data (compare with Fig. 4C); their length difference was 231 nm, corresponding to 38.5 nm per super-repeat. Tmod1 was also localized at two different positions, 962 and 1195 nm from the Z-disk (Fig. 4, E and F). The difference in the positions of the Tmod epitopes suggests the simultaneous presence of two thin-filament populations with 233-nm difference in length. We also used transmission electron microscopy (TEM) to study the sarcomeric ultrastructure of the compound-Het EDL. Two H-zones could be discerned per half sarcomere (fig. S6C), supporting the presence of two distinct thin-filament populations of different length.

TFL adjustments beyond the reach of nebulin

To assess whether the EDL findings can be generalized, we studied diaphragm and soleus muscles, important muscle types specialized for long-lasting contractile activity fueled by oxidative phosphorylation. Nebulin length in diaphragm muscle is similar to that of the EDL in all three genotypes (Fig. 6, A and B). However, unlike in EDL, thin filaments in WT diaphragm protrude far beyond the N terminus of nebulin (Fig. 6C): There is a nebulin-free distal thin-filament segment in WT diaphragm that is 134 nm (Tmod4-based) or 142 nm (phalloidin-based). TFL was reduced by 72 nm in Hom Neb$^{\Delta S9-11}$ and increased by 45 nm in Hom Neb$^{DupS9-11}$ diaphragm. Compared to the EDL, the TFL change was attenuated in the diaphragm of the

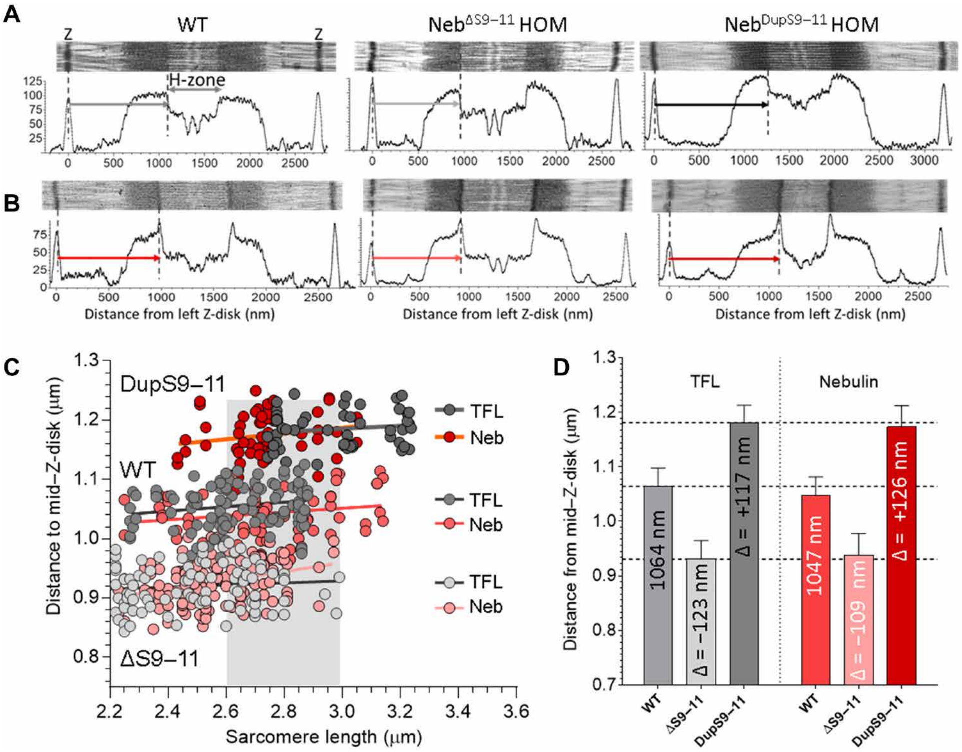

Fig. 5. Nebulin length and TFL measured by TEM and IEM on EDL muscle. (**A**) Top: Example TEM micrographs of skinned muscles from WT and Hom Neb$^{\Delta S9-11}$ and Hom Neb$^{DupS9-11}$ mice. Bottom: TFL was measured using densitometry and determining the distance between the middle of the Z-disk and the H-zone. (**B**) Top: Example IEM micrographs using an N-terminal nebulin antibody. Bottom: Nebulin length was determined using densitometry and determining the distance between the middle of the Z-disk and the nebulin N-terminal epitope in WT, Hom Neb$^{\Delta S9-11}$, and Hom Neb$^{DupS9-11}$ skinned fiber bundles. (**C**) SL dependence of length of nebulin and TFL. (**D**) Mean TFL and nebulin length in the 2.6- to 3.0-μm SL range. The dashed horizontal lines correspond to the average TFL of each genotype. (measurements were corrected for shrinkage; see Materials and Methods for additional). No significant differences between TFL and nebulin length were found (one-way ANOVA with Sidak multiple testing correction).

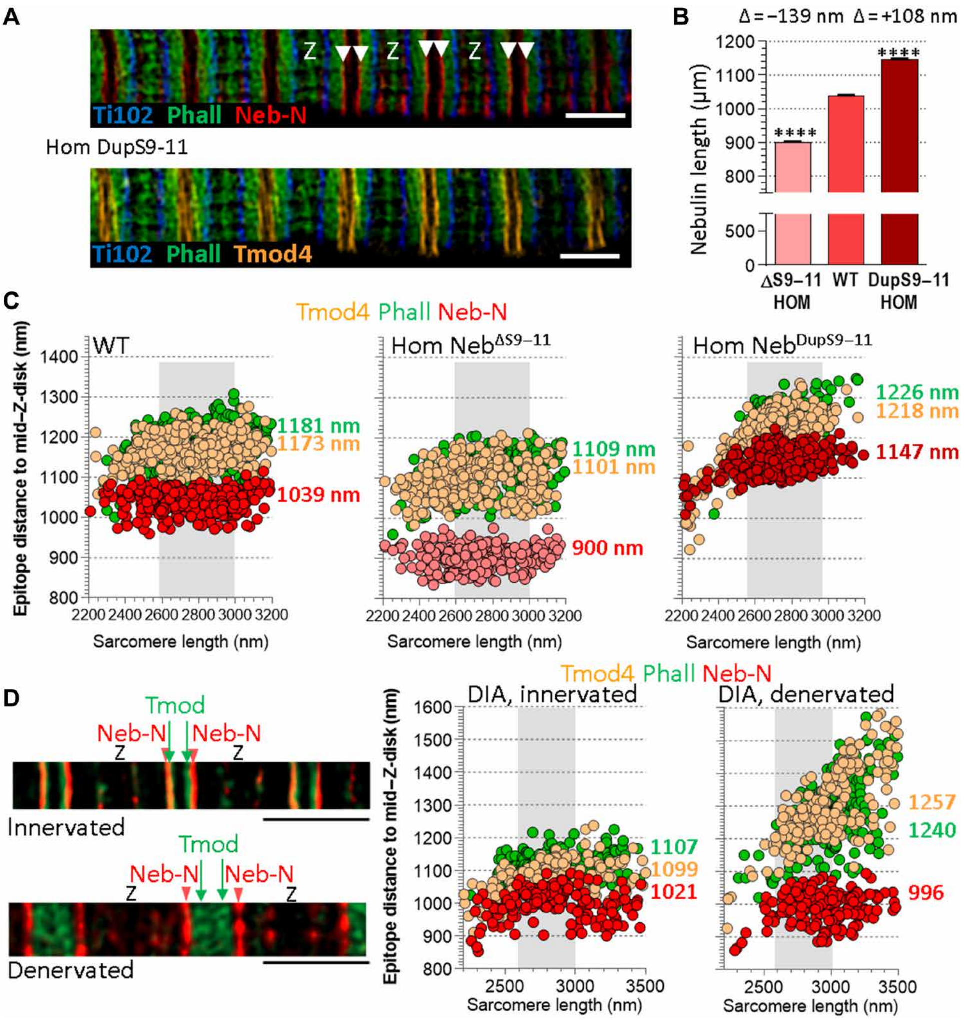

Fig. 6. Thin-filament and nebulin lengths in diaphragm (DIA) muscle. (**A**) Example images showing the same area of a Hom Neb$^{DupS9-11}$ diaphragm muscle. Top: Ti102 (A-band, blue), phalloidin (green), and nebulin N-terminal antibody (red); bottom: Ti102 (A-band, blue), phalloidin (green), and Tmod4 (orange). White arrowheads mark the N terminus of nebulin. Scale bars, 2 μm, Z, Z-disk. (**B**) Nebulin length (average ± SEM in SL 2.6- to 3.0-μm range). The numbers show the difference compared to WT. (**C**) SL dependence of the TFL distance or nebulin N terminus to middle of Z-disk. The numbers represent the mean epitope distance in nanometers, averaged in the 2.6- to 3.0-μm SL range (gray background). (**D**) TFLs in diaphragm undergoing unilateral diaphragm denervation (UDD). In this model, the right diaphragm is denervated and as a result is passively stretched by ~25%. The left diaphragm remains innervated and continues to actively shorten. Left: Example SR-SIM images of diaphragm muscle sections. Red arrowheads mark the N terminus of nebulin. Scale bars, 2 μm. Middle and right: SL dependence of the thin-filament and nebulin length in the innervated side (middle) and denervated side (right) of the diaphragm. The numbers represent the mean values in nanometers, averaged in the 2.6- to 3.0-μm SL range (gray background). The proximal nebulin-containing thin-filament segment is largely unchanged (as reflected by the similar nebulin epitope distances), but the distal nebulin-free segment is longer in the denervated side (Tmod4 and phalloidin distances increased by ~150 nm) [(B) Graph is means ± SEM. ANOVA. ****$P < 0.0001$ in comparison versus WT].

genetically targeted animals as indicated by the reduced slope of the TFL-nebulin length relationship (0.48).

On the basis of a recent diaphragm study that revealed a reduced TFL in a mouse model with a shortened sarcomere-length working range (*22*), we hypothesized that the nebulin-free segment of the thin filament allows for length adjustments in response to changes in SL. This hypothesis was tested by using a surgery model in which the SL operating range of the diaphragm muscle is abruptly increased. In this model, the phrenic nerve that innervates the right side of the diaphragm is transected (unilateral diaphragm denervation, UDD), causing the denervated hemi-diaphragm to passively lengthen by ~25% with each breath, whereas the innervated contralateral side continues to contract (*23*). Thirty hours after surgery, the nebulin lengths were similar in the innervated and denervated sides, but thin filaments of the denervated diaphragm had increased in length, as shown by both the Tmod4 and phalloidin results (Fig. 6D). Thus, it appears that the nebulin-free segment of the thin filament adjusts TFL in response to changes in SL.

Next, we studied soleus muscle as an example of a slow peripheral muscle. Nebulin length in the genetically targeted homozygous animals was generally in accordance with the deletion or insertion of three super-repeats (Fig. 7, A to C). However, in all genotypes, the N terminus of nebulin was consistently ~40 nm further from the Z-disk in the soleus muscle compared to EDL muscle (e.g., in WT 1070 nm in soleus and in EDL 1028 nm). This is likely due to the high incorporation level of Z-disk exons in soleus muscle, the only

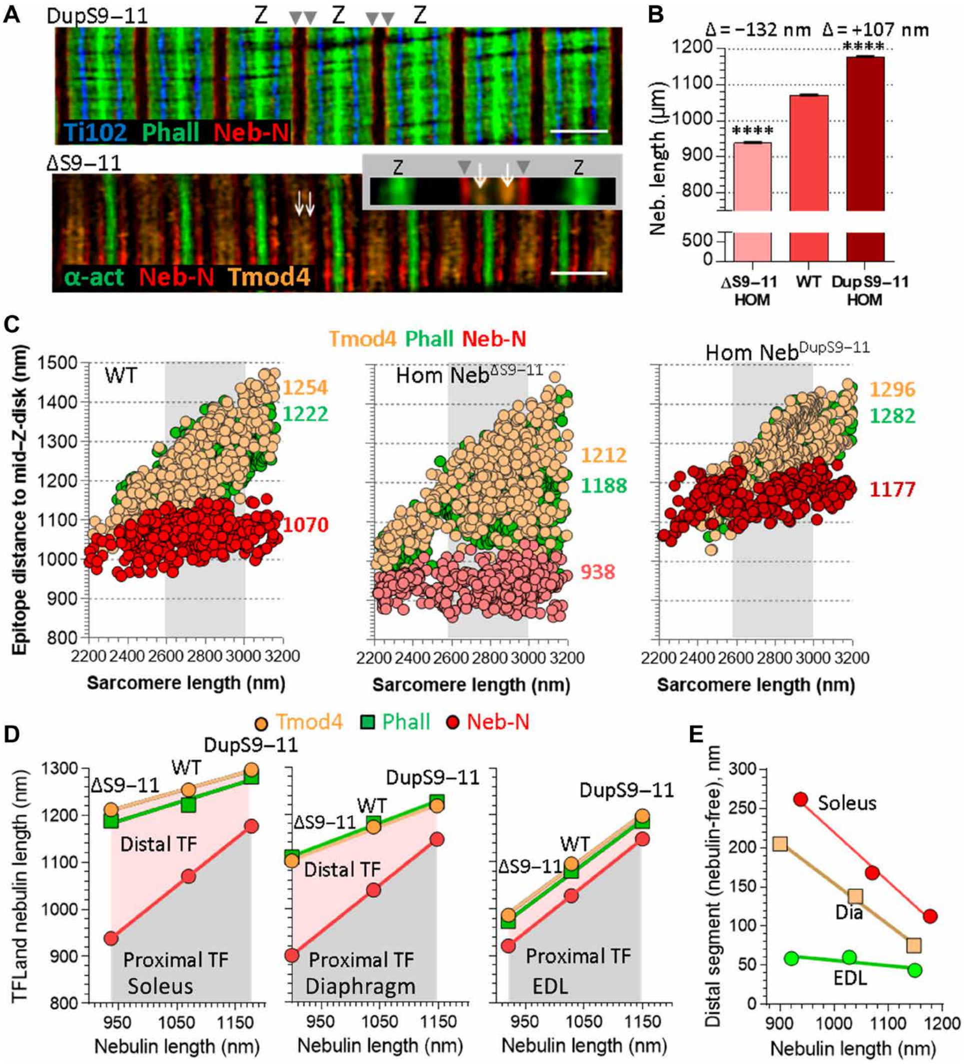

Fig. 7. Thin-filament and nebulin lengths in soleus muscle. (**A**) Example SR-SIM images. Top: Hom Neb$^{\text{DupS9-11}}$; Ti102 (A-band, blue), phalloidin (green), and nebulin N-terminal antibody (red). Gray arrowheads mark the N terminus of nebulin. Bottom: Hom Neb$^{\Delta \text{S9-11}}$; α-actinin (Z-disk, green), nebulin N-terminal antibody (red), and Tmod4 (orange). Tmod4 (white arrow) is localized distal from Neb-N (gray arrowhead). Scale bars, 2 μm, Z, Z-disk. Inset: enlarged sarcomere with epitope localizations emphasizing the proximal nebulin-containing and distal nebulin-free segment of the thin filament. (**B**) Nebulin length (average ± SEM). (**C**) SL dependence of the TFL and nebulin epitope distances. The numbers represent the mean epitope distance in nanometers, averaged in the 2.6- to 3.0-μm SL range (gray background). The numbers show the difference compared to WT. (**D**) TFL versus nebulin length. The distal thin-filament segment (nebulin free) varies in size in the different muscle types. It is large and responds to the length of nebulin in the soleus, it is small and does not respond to the length of nebulin in EDL and is intermediate in the diaphragm. Note that the SEM bars are merged into the actual data points. (**E**) Relation between distal thin-filament segment (nebulin-free) and proximal thin-filament segment (nebulin-containing). [(B) Graph is means ± SEM. ANOVA. $^{****}P < 0.0001$ in comparison versus WT].

area within the nebulin transcript where major PSI differences are found (see above).

The WT soleus featured a ~170-nm nebulin-free distal thin-filament segment, resulting in a total TFL of ~1235 nm (Fig. 7C, left panel). Total TFL was shortened by ~40 nm in Neb$^{\Delta \text{S9-11}}$ and increased by ~50 nm in Hom Neb$^{\text{DupS9-11}}$ (Fig. 7C, middle and right panels). These values reveal a more pronounced attenuation in the expected change in TFL based on nebulin length alone and as compared to the finding in the diaphragm. This is reflected by a further reduction in the slope of the TFL-nebulin length relationship compared to the diaphragm (from 0.48 in the diaphragm to 0.39 for Phall and 0.35 for Tmod).

The dependence of TFL on the length of nebulin is shown in Fig. 7D, for soleus (left), diaphragm (middle), and EDL (right). The soleus contained the longest distal thin-filament segment (nebulin free), the EDL contained the smallest distal segment, and the diaphragm was intermediate. Plotting the length of the distal segment against that of the proximal segment (nebulin containing) revealed an inverse relationship (Fig. 7E). Thus, the distal nebulin-free thin-filament segment varies in length in the different genotypes and, furthermore, partially compensates for the length change of the nebulin-containing segment.

Regulating the nebulin-free distal thin-filament segment in diaphragm and soleus muscle

To gain insights into how the length of the nebulin-free distal thin-filament segment might be controlled, the earlier described transcript studies on thin-filament pointed-end interacting proteins were extended with Western blot studies (Fig. 8A, left and bottom). Lmod2 expression levels were significantly higher ($P < 0.0001$) in soleus than EDL muscle with expression in the diaphragm at an intermediate level. Lmod3 expression also varied with muscle type similar to Lmod2, although the differences were not as pronounced as for Lmod2. Tmod1 and Tmod4 levels varied with muscle type as well, and both were modestly higher in soleus than in EDL or diaphragm.

Considering that Tmods are likely to play a role in keeping thin filaments short (*2*), the observed muscle-type dependence of Tmod expression (i.e., higher Tmod expression in muscle types that have a longer distal segment) is inconsistent with a dominant role for Tmod in regulating the length of the distal thin-filament segment. Instead, Lmod might perform this function (*2*, *24*). Lmod2 expression analyzed in a two-way ANOVA revealed in the soleus muscle a genotype effect with a multiple comparison indicating a significant ($P < 0.0001$) reduction in Lmod2 expression in the $\mathrm{Neb}^{\mathrm{DupS9-11}}$ compared to the $\mathrm{Neb}^{\Delta \mathrm{S9-11}}$ (Fig. 8A, bottom left). The expression levels of Lmod2/3 and Tmod1/4 in soleus muscle were also plotted against the length of the nebulin-free distal thin-filament segment, which revealed the strongest correlation for Lmod2, i.e., as Lmod2 expression increased, the nebulin-free distal segment lengthened (Fig. 8B).

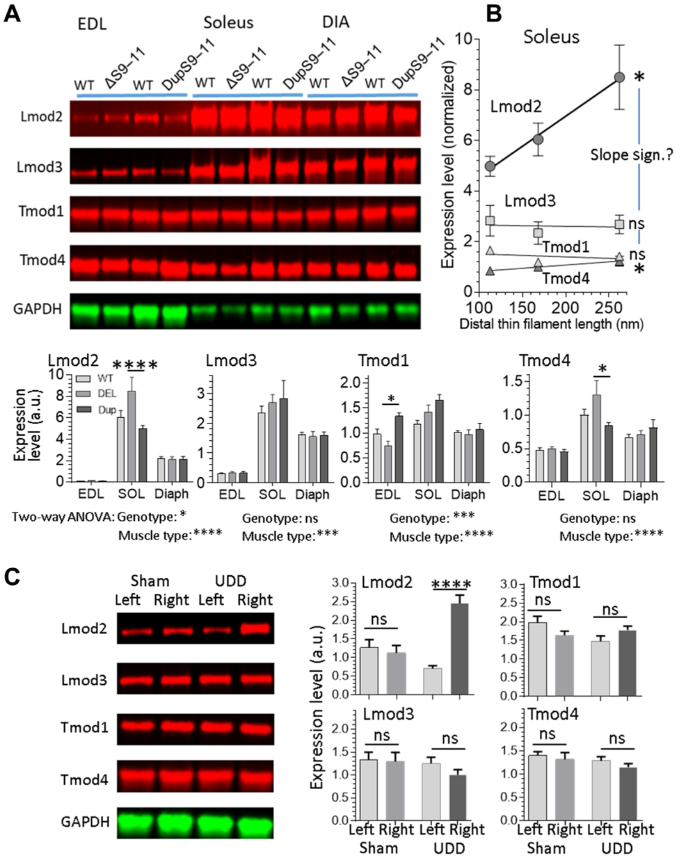

Fig. 8. Expression levels of thin-filament proteins Lmod2, Lmod3, Tmod1, and Tmod4. (**A**) Analysis in EDL, soleus, and diaphragm muscle of WT, Hom $\mathrm{Neb}^{\mathrm{DupS9-11}}$, and Hom $\mathrm{Neb}^{\Delta \mathrm{S9-11}}$ mice. Left: Example Western blots and bottom: expression levels [normalized to glyceraldehyde-3-phosphate dehydrogenase (GAPDH)]. The expression level of Lmod2 is very low in EDL muscle, ~50-fold higher in soleus and intermediate in diaphragm. In addition, Lmod2 expression is lower in $\mathrm{Neb}^{\mathrm{DupS9-11}}$ than in $\mathrm{Neb}^{\Delta \mathrm{S9-11}}$ mice. (**B**) Expression levels of Lmod2/3 and Tmod1/4 in soleus muscle in the three genotypes plotted against the length of the distal thin-filament segment (nebulin-free). The slopes of the regression lines are significant for Lmod2 and Tmod4). (**C**) Expression analysis in left and right sided diaphragm muscle of sham-operated mice and UDD mice where the left side continues to contract but the right side is denervated for 30 hours. Lmod2 is ~three-fold up-regulated in the denervated side ($P < 0.0001$). [(A) regular two-way ANOVA with multiple comparison testing using Tukey: $^{*}P < 0.05$ and $^{****}P < 0.0001$. (B) linear regression analysis. (C) One-way ANOVA with multiple comparison testing with Tukey correction. $^{****}P < 0.0001$ in comparison to left side, left. Graphs show means ± SEM). a.u., arbitrary units.

The unilaterally denervated diaphragm where the nebulin-free distal thin-filament segment has increased in length (introduced above) was also studied. Results show that in the denervated side, Lmod2 was ~3-fold up-regulated with no significant changes in the other proteins (Fig. 8C). Thus, although Lmod2 has been assumed hitherto to regulate TFL in only cardiac muscle where nebulin is absent (*2*, *12*, *24*), our findings suggest that Lmod2 could also play a role in skeletal muscle by regulating the length of the distal thin-filament segment.

To test the hypothesis that Lmod2 is involved in TFL regulation in skeletal muscle by regulating the length of a distal nebulin-free segment, a conditional Lmod2 knockout (KO) mouse model was used in which the start site containing exon 1 was floxed (*12*). The soleus muscles of adult cLmod2 KO mice were intramuscularly injected with a Cre–adeno-associated virus (AAV9) (see Materials and Methods for details) to trigger KO of Lmod2 expression in this muscle specifically. Three weeks later, the Lmod2 protein level was reduced by ~95% without affecting Lmod3, Tmod1, and Tmod4 protein levels (Fig. 9A). The length of the nebulin-free segment, both when measured with Tmod4 and phalloidin, was found to be greatly reduced in the absence of Lmod2 (Fig. 9B).

As an additional test for whether the correlation between Lmod2 expression and the length of the distal thin-filament segment is causative, the UDD method was used on cLmod2 KO mice. As shown above, the denervated hemi-diaphragm of WT mice up-regulates Lmod2 and increases the length of the distal thin-filament segment (Figs. 6D and 8C); if there is a causal relationship, then the denervated hemi-diaphragm of cLmod2 KO mice is predicted to not increase TFL. Protein studies showed that the Lmod2 expression level in the denervated diaphragm of cLmod2 KO mice was reduced >95% (as expected) with no effects on Lmod3 and Tmod 4 expression, a modest increase in Tmod1 expression in denervated cLmod2 KO diaphragm, and no Tmod1 expression difference in cLmod2 KO compared to WT denervated diaphragm (Fig. 10A). In contrast to the denervated diaphragm in WT mice, the distal thin-filament segment was short in the denervated cLmod2 KO diaphragm (Fig. 10, B and C). These in vivo data support that in skeletal muscle Lmod2 plays an essential role in regulating the length of the nebulin-free distal thin-filament segment.

DISCUSSION

To critically investigate the role of nebulin in TFL regulation, two mouse models were created that produce shortened or lengthened nebulin molecules. Both models are viable and incorporate the length variants of nebulin normally in their sarcomeres. Our results resolve why there is compelling data in the literature for and against the molecular ruler hypothesis of TFL regulation. We found that in some muscle types, nebulin functions as a molecular ruler and that in others nebulin is part of a dual nebulin/Lmod2 length-regulation mechanism.

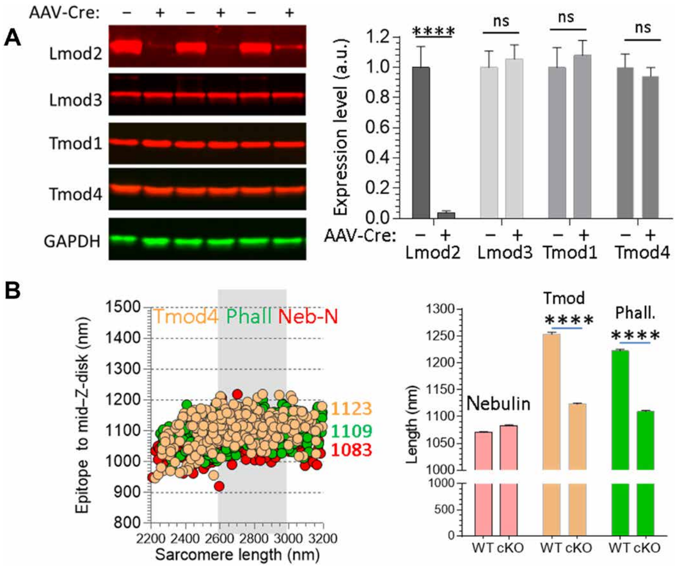

Fig. 9. Effect of deleting Lmod2 on TFL in soleus muscle. Conditional Lmod2 KO mice were injected with an adeno-associated virus (AAV)–Cre virus, and 3 weeks later, the soleus muscles were harvested. Muscles were analyzed for protein expression and TFL measurement. (**A**) Example Western blots (left) and expression levels (right, values normalized to GAPDH and the mean value in control mice) in soleus muscle reveal a ~95% reduction in Lmod2 levels in soleus muscle of AAV-Cre–treated Lmod2 conditonal KO (cKO) mice, without affecting Lmod2, Tmod1, and Tmod4 expression levels. (**B**) Left: Length of nebulin and lengths of thin filaments in soleus muscle, based on Tmod4 and phalloidin localization, as a function of SL. In the 2600- to 3000-nm SL range, the nebulin length and TFL are ~1100 nm. (B) Right: Comparison between WT (same data as in Fig. 7C) and Lmod2 cKO soleus treated with AAV-Cre shows a highly significant reduction in TFL in Lmod2 cKO soleus muscle both when measured with Tmod4 antibody and phalloidin [analyzed with one-way ANOVA with multiple testing (Sidak) correction; $^*P < 0.05$; $^{****}P < 0.0001$. Graphs are means ± SEM).

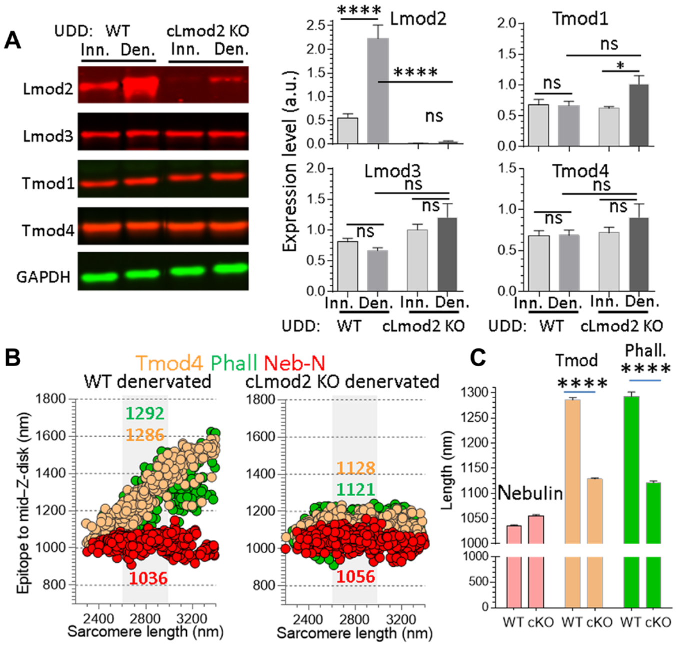

Fig. 10. Effect of deleting Lmod2 on TFL in denervated diaphragm muscle. Conditional Lmod2 KO mice were injected with an AAV-Cre virus; 3 weeks later, UDD surgery was performed; and 30 hours later, the innervated and denervated hemi-diaphragms were collected. UDD was also performed on WT mice. The innervated (Inn.) and denervated (Den.) hemi-diaphragms were both analyzed for protein expression; the denervated muscles were also used for nebulin length and TFL measurements. (**A**) Example Western blots (left) and expression levels (right, values normalized to GAPDH and the mean value in control mice) reveal a >95% reduction in Lmod2 levels in both innervated and denervated diaphragm muscles of AAV-Cre–treated Lmod2 cKO mice, without affecting Lmod3 and Tmod4 expression levels. Tmod1 was slightly increased in the denervated diaphragm of the cLmod2 KO mice compared to the innervated side but was not different when compared to WT mice. (**B**) Length of nebulin and length of thin filaments, based on Tmod4 and phalloidin localization, as a function of SL. The shown values are mean values in the 2600- to 3000-nm SL range. In WT denervated diaphragm (left), the thin-filament pointed-end extends far beyond nebulin and in cLmod2 KO denervated muscle (right), this is not the case. (**C**) Comparison between WT and Lmod2 cKO denervated diaphragm. Lmod2 deficiency results in much shorter thin filaments (~12%) in denervated diaphragm (analyzed with one-way ANOVA with multiple testing (Sidak) correction; $^*P < 0.05$ and $^{****}P < 0.0001$. Graphs are means ± SEM).

Below, we discuss these findings and focus on the functional advantage of using the strict nebulin mechanism in muscle types that require speed and the dual nebulin/Lmod2 mechanism in muscles specialized for contractile activity that is long lasting. We also discuss the clinical implications of our findings.

Exon usage in the three studied skeletal muscle types revealed that most exons in the 25 super-repeat region of the *Neb* gene were maximally expressed, suggesting limited differential splicing. An exception is exons 65 to 78 that were expressed at 60 to 90% of maximal (Fig. 2A). Analyzing splice junctions revealed that always an integer number of super-repeats was spliced out (fig. S3D), indicating that the exclusion of full super-repeats is tolerated but not partial super-repeats. This conclusion is consistent with previous work on a model that deletes exon 55 (*Neb*$^{\Delta ex55}$ mouse) (*25*), replicating a founder mutation that causes nemaline myopathy (*26*). Mice die soon after birth and express extremely low levels of nebulin protein (*25*), which has been explained by the partial deletion of a super-repeat that causes a mismatch between nebulin and other thin-filament proteins that are regularly spaced along the thin filament, increasing the sensitivity of nebulin to proteolysis (*25*). The Neb$^{\Delta S9-11}$ model survives into adulthood while producing normal nebulin protein levels, despite that exon 55 is among the deleted exons. Thus, the deletion of an integer number of nebulin super-repeats is tolerated, likely because it maintains the phase between the shortened nebulin and the actin filament. These insights are important for treating nemaline myopathy caused by mutations in *Neb* exons because they suggest that only exon skipping of entire super-repeats is a suitable therapeutic approach.

The difference between the nebulin lengths of the Hom Neb$^{\Delta S9-11}$ and Hom Neb$^{DupS9-11}$ was in all three muscle types ~230 nm. This value is in good agreement with the 231-nm length difference (38.5 nm per super-repeat) found between the long and short nebulin isoforms expressed in the compound-Het Neb$^{\Delta S9-11/DupS9-11}$ EDL (Fig. 4E) and the 116-nm difference (38.7 nm per super-repeat) in the Het Neb$^{\Delta S9-11}$ EDL (Fig. 1F). On the basis of the sequence analysis and protein binding studies, nebulin has been proposed to interact with both actin and tropomyosin by following the thin-filament helix with each of its super-repeats spanning 38.5 nm, similar to tropomyosin/troponin periodicity (*5*, *6*, *8*, *27*). Thus, the findings of the present work support a model in which a nebulin super-repeat spans 38.5 nm, and each simple repeat spans 1/7 of this distance, or 5.5 nm (corresponding to the size of an actin monomer).

The measured length of nebulin in WT mice was 1035 nm in EDL (mean of SR-SIM and IEM-based values) and 1070 nm in soleus (SR-SIM). These values are substantially longer (by ~100 to 200 nm) than the nebulin lengths published by others for the mouse EDL and soleus muscles (*28*, *29*) (all studies measured the distance from the middle of the Z-disk to nebulin's N terminus, using the same antibody as used here). Are the long nebulin lengths that we obtained compatible with the nebulin exon composition revealed by RNA-seq? The typical nebulin transcript was found to contain 208 simple repeats in soleus muscle and 199 in EDL muscle, resulting in a predicted total length of 1144 nm (208 × 5.5) and 1094 nm (199 × 5.5), respectively. These values are longer than the measured 1070 nm (soleus) and 1035 nm (EDL). The used nebulin length measurement method, however, does not precisely mark the ends of the molecule. The N-terminal nebulin antibody is a polyclonal against domains M1-M3, and the measured antibody position likely reflects the middle of M1-M3, i.e., 8 nm short of nebulin's N terminus. In addition, measurements assume that nebulin's C terminus is at the middle of the Z-disk, while in reality, nebulin is likely to penetrate the Z-disk (*30*, *31*). This will underestimate the measured length of nebulin by half of the Z-disk thickness, i.e., 50 nm in soleus and 25 nm in EDL (*18*, *19*). Hence, the corrected measured nebulin length is 1128 nm for soleus (1070 + 8 + 50) and 1078 nm for EDL (1035 + 8 + 25). These values are within 16 nm of those predicted based on transcript analysis, validating the results of the present study. The short nebulin lengths that were published earlier (*28*, *29*) might be due to various factors that include genetic strain and/or age of the mice studied (*28*). It is also possible that the previous work on mouse muscles studied sarcomeres that were relatively short. Nebulin and TFLs have to be measured at long SLs where the thin filaments have been pulled away from the M-band and where the TFL and the nebulin length are independent of SL. Doing so reveals that nebulin is ~1078 nm in EDL and ~1128 nm in soleus muscle.

In EDL muscles, TFL followed nebulin length with identical results when TFL was measured with Tmod antibodies or phalloidin (Fig. 4B) or TEM (Fig. 5D). The direct comparison between the proximal and distal Tmod epitopes in the compound-Het EDL revealed a 233-nm distance, matching the length difference between the short and long nebulin (Fig. 4F). These findings support that nebulin is a TFL ruler in EDL muscle.

Admittedly, in the EDL muscles of all three genotypes, thin filaments extend ~50 nm beyond nebulin (Fig. 4B). It is possible that this represents a ~50-nm nebulin-free segment that does not respond to shortening/lengthening of nebulin. An alternative explanation is as follows. There are 72 residues N-terminal from M1 that can span as much as ~17 nm (see Materials and Methods). In addition, the N-terminal nebulin antibody can bind anywhere within its M1-M3 antigen sequence, the real N terminus of nebulin might be as much as ~33 nm (~17 + 3 × 5.5) distal from the position of the antibody epitope. This is still shorter than the observed ~50-nm distance toward the thin-filament pointed-end (as measured with the Tmod antibody) and suggests a short nebulin-free distal thin-filament segment in EDL muscle of at least ~20 nm. Since this occurs equally in all three genotypes, we propose that this reflects the precise structural arrangement by which nebulin, tropomyosin, and Tmod interact at the thin-filament pointed-end to terminate the thin filament.

In a previous study, the number of nebulin super-repeats was altered by reducing endogenous nebulin from chicken myotubes (nebulin in chicken contains 23 super-repeats) and then expressing a mini-nebulin that contained nebulin's N terminus, four super-repeats (i.e., 19 less than normal), and the C terminus (*32*). The obtained result was different from the present study in that TFL did not follow the length of nebulin. Expressing mini-nebulin shortened actin filaments by 240 nm, much less than the expected 732 nm (19 × 38.5 nm). A standout difference from the present study is the much larger reduction in the number of super-repeats (19 versus 3), and as stated by Pappas *et al.* (*32*), it is possible that due to the extreme short length of mini-nebulin, the normal role of nebulin in regulating actin filament length is rendered ineffective by the large amount of G-actin present in the myotubes. Other differences between the studies are that Pappas *et al.* expressed a human mini-nebulin with tags on both ends (hemagglutinin and green fluorescent protein) and used chicken cultured myotubes from which endogenous nebulin was transiently knocked down using small interfering RNA. In the present study, a mouse model was used in which the endogenous nebulin gene is permanently altered, no tags are used, and the muscles develop and function normally in vivo. Thus, the model systems are very different, and this is likely to contribute to the differing result.

Our data support that in fast muscle of the mouse, nebulin functions as a TFL ruler. How might nebulin accomplish this? Depolymerization studies and FRAP (fluorescence recovery after photobleaching) assays have shown that nebulin stabilizes F-actin and enhances the binding of tropomyosin along the thin filament and of Tmod to the thin-filament pointed-end (*32*). This is consistent with nebulin's actin and tropomyosin binding sites that are present in each super-repeat (*5*, *6*, *27*, *33*). Thus, it stands to reason that the length of the thin filament varies with the number of super-repeats.

TFL in mouse diaphragm and soleus, however, did not strictly follow the nebulin length, which manifested as a proximal thin-filament segment that contains nebulin and a ~100 to 250-nm distal segment that is nebulin-free (Fig. 6D). These data support earlier work where this distal segment was first reported (*14*, *34*). Here, we show for the first time that the length of the distal nebulin-free segment responds to the length of nebulin as it is increased in $\mathrm{Neb}^{\Delta S9-11}$ and decreased in $\mathrm{Neb}^{\mathrm{DupS9-11}}$ mice (Fig. 6E), resulting in an attenuated TFL change in response to the altered nebulin length. The diminished role of nebulin in setting total TFL is reflected in the slope of the TFL-nebulin length relation that is ~0.5 for diaphragm and ~0.4 for soleus (Fig. 4D).

How is the length of the distal thin-filament segment that is nebulin-free controlled? Various mechanisms have been proposed by others that include pointed-end dynamics involving Tmod, bare-zone associated proteins that act as targeting signals for Tmod1 and that halt thin filament elongation once the thin-filament pointed-end reaches the bare zone, and altered actin filament properties that originate from the nebulin-containing segment of the thin filament and that propagate toward the pointed-end [for reviews, see (*14*, *35*)]. Our present work suggests a novel explanation that is based on the positive and causal relation between Lmod2 levels and the length of the distal nebulin-free segment. Important evidence for this conclusion comes from the experiments with the cLmod2 KO model that revealed that knockdown of Lmod2 greatly shortened the distal segment in soleus muscle and abolished the increase in the length of the distal thin-filament segment in denervated diagram muscle (Figs. 9 and 10). Lmod2 has been shown to play a role in TFL regulation in cardiac muscle but was assumed unimportant in skeletal muscle (*2*, *12*, *24*). This assumption is likely due to the earlier focus on fast-twitch skeletal muscle where Lmod2 expression is very low (which we confirmed), and, therefore, an important Lmod2 function seemed unlikely. However, our studies convincingly show that Lmod2 is highly expressed in soleus and diaphragm muscle and, importantly, that Lmod2 plays a dominant role in regulating the nebulin-free distal thin filament in skeletal muscle. Lmod2 might exert these effects through antagonizing the capping function of Tmod1 (*11*, *36*) or by binding to the side of the thin filament (*37*) and stabilizing the distal segment (analogous to nebulin). We envision that when Lmod2 expression is increased, Lmod2 effectively competes with Tmod1 and dislodges it from the pointed-end, promoting elongation of the thin filament with Lmod2 stabilizing the nebulin-free thin-filament segment that is formed. As the nebulin-free segment grows, the pool of free Lmod2 falls and when a sufficiently low level is reached, Tmod1 will be able to cap the pointed-end again. How Lmod2 expression is regulated and how changes in the SL range in the denervated hemidiaphragm lead to altered Lmod2 expression is an important topic for future research. Considering the Lmod2 up-regulation in the denervated diaphragm (Fig. 8C), the underlying mechanism in not dependent on calcium or crossbridge interaction. In summary, the present work supports that the length of the nebulin-free distal thin-filament segment in skeletal muscle is regulated by Lmod2.

Is the dual length-regulating system (nebulin/Lmod2) functionally advantageous? Due to the enormous size of nebulin and its many complex functions involving multiple protein interactions, including some deep inside the Z-disk (*31*, *38*), the replacement of nebulin molecules is expected to be a complex and slow process. Thus, rapidly adjusting TFL, if the need arises, through exchanging nebulin size-variants is likely to be inefficient and slow. In contrast, Lmod2 is a small, dynamic, and much less complex molecule that is expected to be able to respond quickly if TFL adjustments are needed. Evidence for this was obtained in the UDD model in which the SL was abruptly increased in the denervated-half of the diaphragm and Lmod2 protein was up-regulated within 30 hours, resulting in elongation of the thin-filament distal segment. In this model, myosin interaction with the nebulin-free segment of the thin filament is not mandatory. Thus, the nebulin/Lmod2 dual-regulatory system allows for rapid TFL adjustment.

The prominence of the dual length-regulation system in soleus and diaphragm might relate to their long-lasting contractions (soleus muscle is an anti-gravity postural muscle that can contract for many hours and the diaphragm contracts with each breath, for life) and therefore they need to be as efficient as possible. By having a prominent distal thin-filament segment, muscles can develop maximal force in long sarcomeres and this improves the efficiency of force generation (fewer sarcomeres per unit length of muscle are required). Furthermore, if Lmod2 can rapidly adjust the TFL to changes in SL, then force levels and the efficiency of contraction can be maintained at the desired optimum. In fast contracting muscle (e.g., EDL), on the other hand, nebulin functions as a molecular ruler that controls thin filaments at a defined and relatively short length. This makes the optimal SL for force production relatively short, the number of sarcomeres per unit length of muscle relatively high, and consequently the shortening speed of whole muscle (the sum of all sarcomeres in series) will be high.

The Lmod2 findings of the present work should be further investigated in future studies, for example, by experimentally increasing Lmod2 protein in the soleus muscle and establishing whether up-regulating Lmod2 is a potential therapeutic approach for treating diseases in which skeletal muscle thin filaments are reduced in length. A prime example of a disease with reduced TFL is nebulin-based nemaline myopathy (*1*, *18*, *39*); up-regulating Lmod2 is predicted to lengthen thin filaments and improve force production in these patients. Our work is also relevant for dilated cardiomyopathy patients with mutations in Lmod2 (*3*), as cardiac-specific treatments [e.g., heart transplantation (*3*)] would still leave patients vulnerable to developing skeletal muscle myopathies, a topic that also requires future studies.

In summary, experiments with unique and powerful mouse models showed that nebulin functions as a molecular ruler in fast-contracting muscle, thereby ensuring well-defined thin filaments of a uniform and relatively short length and promoting a high speed of shortening. In muscles specialized for long-lasting or frequent contractions, nebulin's ruler function is augmented by Lmod2 that makes thin filaments long and tunable (without requiring nebulin's replacement), promoting efficiency of contraction. In skeletal muscle, TFL regulation follows function.

MATERIALS AND METHODS

Study design

Overview

To study the role of nebulin in thin-filament length regulation and test the hypothesis that nebulin is a TFL ruler, mouse models were created that express shortened or lengthened nebulin molecules. To establish whether the gene targeting experiments have unintended consequences, exon-level transcript studies, protein expression studies, and general characterization studies were conducted. The mouse models were then used to study whether and how TFL is altered. Nebulin length and TFL were measured in three muscle types (two distinct peripheral muscles, EDL and soleus, and diaphragm muscle) using SR-SIM and IEM. Since TFL affects the descending limb of the F- SL relation (*40*), with a predicted shift along the SL axis by twice the TFL, functional studies were also performed. Since results established a nebulin-free distal thin-filament segment in diaphragm and soleus muscle, we tested whether this distal segment responds to altering the physiological SL range. For this, a UDD model was used. Pointed-end binding proteins were also studied, and because obtained results suggested that Lmod2 might play a role in TFL regulation in slow muscle types, an Lmod2 conditional KO was used in which Lmod2 was deleted in soleus muscle of adult mice and its effect on TFL was studied. The number of animals needed for the various experiments was calculated wherever possible based on power calculations, with the significance level set at $P < 0.01$, and assuming variance similar to that of our previous studies. The method for calculating the number of required mice is according to Glantz and Slinker: Primer of applied regression and ANOVA, McGraw-Hill Inc., 2002. The obtained result was not altered during the course of the experiments, no rules for stopping data collection in advance were defined, and all obtained data were included in the study. All data represent independent experiments (i.e., no technical replicates), and the number of mice and independent samples is reported below for each figure. Sample randomization and blinding of the investigator were applied, and investigators were unaware of the genotype of the animals during any stage of data collection. The results were obtained over a period of ~3 years, from multiple different litters per genotype as defined in Results section. The details of the methods that were used and the statistical analyses are described below.

Generation of mouse models

For the Neb$^{\Delta S9-11}$ mice, a targeting vector was designed that deleted exons 53 to 64 [(15,326 base pair (bp) deletion: chr2:52,250,795-52,266,120], encoding three super repeats. The Osdd vector (providing

TK for negative selection) was used, and homology arms (4 kb left and 3.5 kb right) allowed the replacement of the deleted sequence with a FRT (flippase recognition target)–flanked *neo*^{R}-positive selection cassette. For generating the Neb$^{\text{DupS9–11}}$ mice, a targeting vector was designed using the Osdd vector with a 3.4 kb left-arm and 3.5 kb right-arm of homology. This vector replaces 1347 bp (chr2:52,250,794-52,252,140) including exon 64 with a 2.8-kb synthetic complementary DNA (cDNA) fragment with exon 64 + exons 53 to 64 (and flanking intronic sequence) followed by a *neo*^{R}-positive selection cassette. Linearized targeting vectors were electroporated into 129S6/SvEvTac cells; five G418-resistant ES cell clones (confirmed to have correctly integrated into the *Neb* gene) were injected into blastocysts, transferred into host mothers, and produced chimeras. Mice were crossed to FlpO [B6.Cg-Tg(Pgk1-flpo)10Sykr/J, no. 11065 the Jackson laboratory] to remove the *neo*^{R} cassette. Mice with the *neo*^{R} cassette removed were backcrossed C57BL/6J (no. 664, the Jackson laboratory) to select FlpO-negative offspring. Mice were backcrossed to C57BL/6J mice for eight generations and used at 2.5 to 3.0 months of age. All mice in this study were maintained in a pathogen-free barrier facility with 14-hour light/10-hour dark cycle with access to water and food ad libitum. All animal procedures were done in accordance with the University of Arizona Institutional Animal Care and Use Committee and followed the U.S. National Institutes of Health (NIH) Using Animals in Intramural Research guidelines for animal use.

RNA sequencing

EDL, soleus, and diaphragm samples were collected from 12-week-old mice. Samples were stored in RNAlater to preserve RNA integrity. Four mice were used per muscle type from WT, Neb$^{\Delta\text{S9–11}}$, and Neb$^{\text{DupS9–11}}$ mice. For RNA extraction, 600 μl of prechilled buffer RLT (RNeasy Fibrous Tissue Mini Kit, Qiagen) with 1% β-mercaptoethanol was added to muscle tissue stored in RNAlater in a 4-ml cryovial. Tissue was disrupted using a rotor-stator homogenizer for 30 s. RNA extraction was performed following the manufacturer's instructions and quantified using a Nanodrop ND-1000 spectrophotometer (Thermo Fisher Scientific). RNA integrity was checked on a 2100 Bioanalyzer (Agilent), and all RNA integrity number scores were confirmed to be ≥8.

For library preparation, ribosomal RNA (rRNA) was depleted from RNA preparations with a NEBnext rRNA depletion kit using 1 μg of total RNA as starting material. Libraries were prepared using the NEBNext Ultra II Directional RNA Library Prep Kit for Illumina following the manufacturer's instructions. RNA was fragmented for 10 min at 94°C. For first strand cDNA synthesis, incubations were for 10 min at 25°C followed by 50 min at 42°C and 15 min at 70°C. For size selection, conditions for an approximate insert size of 300 bp were used. Size-selected libraries were enriched by PCR for 10 cycles and purified using NEBnext sample purification beads. Library quality and insert sizes were checked using a 2100 Bioanalyzer (Agilent). Sequencing was performed on an Illumina Hiseq2500 sequencer using 150-bp paired-end sequencing. The raw data are available (BioProject accession PRJNA613762). Adapters and low quality reads were removed with Trim Galore (www.bioinformatics.babraham.ac.uk/projects/trimgalore/), and reads were mapped to the mouse genome (Release M23 GRCm38.p6) using STAR (*41*) with default settings. Differential genes were determined with DESeq2 (*42*). Genes with Benjamini-Hochberg–adjusted $P < 0.05$ were considered to be differentially expressed. To determine which genes might have an effect on phenotypic differences observed in Nebulin deletion versus duplication models, pathway analysis was performed using the goseq R-package. As input for the analysis, we considered all differentially expressed genes versus a background of all genes with an average of two reads per library. Genes related to muscle structure and function were considered for further testing and confirmation by Western blots.

For calculating inclusion percentages of all exons from nebulin transcripts, inclusion reads (IRs) and exclusion reads (ERs) were counted for each exon based on annotation from Kazmierski *et al.* (*15*). IRs are reads overlapping the exon being investigated, normalized by exon length. ERs are reads either upstream or downstream that support exclusions of the read. From these factors, the following equations were used to calculate the PSI index using the ASpli R-package (*43*)

$$\mathrm{IR}_{i,n} = \frac{\mathrm{IR}_i}{\text{length exon}_i + \text{read length} - 1}$$

$$\mathrm{ER}_{i,n} = \frac{\mathrm{ER}_i}{\text{read length} - 1}$$

$$\mathrm{PSI}_i = \frac{\mathrm{IR}_{i,n}}{\mathrm{IR}_{i,n} + \mathrm{ER}_{i,n}}\%$$

where i is the exon number and n is the normalized read counts. Determination of differential exon usage was performed after adjusting exon counts to gene counts by

$$E^A_{ijk} = \frac{E_{ijk} \times \overline{G}_j}{G_{jk}}$$

where E^A_{ijk} is the adjusted exon count for exon i of gene j in sample k, E_{ijk} is the raw exon count for exon i of gene j in sample k, $\overline{G}_j$ is the mean raw count for gene j for all samples, and G_{jk} is the raw gene count for gene j in sample k.

Read density was calculated by dividing read counts per exon by exon length. To confirm increased read counts of duplicated super-repeats in Neb$^{\Delta\text{S9–11}}$, read density of WT samples was subtracted from Neb$^{\Delta\text{S9–11}}$ samples. To determine significance of differential splicing events, one-way ANOVA tests were applied to PSI values from individual exons of the compared groups with Benjamini-Hochberg multiple testing correction. To check the frequency of exon skipping events in nebulin super-repeat and Z-disk regions, reads spanning splice junctions and skipping at least one exon were counted separately for each skipping event. After analyzing which nebulin exons were skipped, nebulin repeat domains coded by the skipped exons were determined and counted. The percentage of cases where a multiple of seven domains were skipped was calculated separately for super-repeat and Z-disk regions of nebulin.

Tissue-specific Lmod2 KO in soleus muscle

The Lmod2 conditional KO mouse model was used in which exon 1 was floxed [for details on this model, see (*12*)]. Targeted recombination was achieved using an AAV9 that expresses iCre in striated muscle under the control of a tMCK promoter (AAV-tMCK-iCre-WPRE, Vector Bioloabs no. VB5021). While under anesthesia (1 to 2% isoflurane), animals received a direct soleus intramuscular injection using a 30G needle, in doses of 5.0×10^{10} vg per 5-μl volume phosphate-buffered saline (PBS) containing 5% glycerol. Tissues were harvested 3 weeks later for protein analysis and TFL measurements.

Tissue collection and protein analysis

Flash-frozen extensor digitorum longus (EDL), diaphragm (DIA), and soleus (SOL) tissues were pulverized in liquid nitrogen and then solubilized in urea buffer [8 M urea, 2 M thiourea, 50 mM tris-HCl, 75 mM dithiothreitol with 3% SDS, and 0.03% bromophenol blue (pH 6.8)] and 50% glycerol with protease inhibitors (0.04 mM E64, 0.16 mM leupeptin, and 0.2 mM phenylmethylsulfonyl fluoride) at 60°C for 10 min (*44*). Solubilized samples were centrifuged at 13,000 RPM for 5 min, aliquoted, flash-frozen in liquid nitrogen, and stored at −80°C. Nebulin expression analysis was performed on solubilized samples using a vertical SDS-agarose gel system. 1% gels were run at 15 mA per gel for 3:20, then stained using Coomassie brilliant blue, and scanned using a commercial scanner. The previously determined PCR-based genotype of the animal was protein-confirmed based on the mobility of nebulin assuming an approximate WT molecule weight of 750 kDa (*45*). The scanned gels were subsequently analyzed with One-D scan (Scanalytics). The integrated optical density (IOD) of myosin heavy chain (MHC) was determined as a function of loading volume (in a range of five volumes). The slope of the linear relationship between IOD and loading was obtained for each protein to quantify expression ratios. For Western Blotting, solubilized samples were run on a 10% polyacrylamide gel and transferred onto polyvinylidene difluoride membranes using a semi-dry transfer unit (Trans-Blot Cell, Bio-Rad). Blots were stained with Ponceau S to visualize the total protein transferred. Blocking, detection with infrared fluorophore-conjugated secondary antibodies, and scanning followed recommendations for Odyssey Infrared Imaging System (LI-COR Biosciences). The following primary antibodies were used for Western Blotting: anti-nebulin N-terminal (1:2000; rabbit polyclonal; no. 6969, Myomedix), anti-Tmod1 (1:5000; X523-X524, rabbit polyclonal; no. 8627, BioGenes), anti-Tmod4 (1:1000; X527-X528, rabbit polyclonal; no. 8629, BioGenes), anti-Lmod2 (1:500; rabbit polyclonal, sc-135491, Santa Cruz Biotechnology), and anti-Lmod3 (1:1000; rabbit polyclonal; 14948-1-AP, Proteintech). Protein expression was normalized to glyceraldehyde-3-phosphate dehydrogenase (GA1R, mouse monoclonal; 1:5000; Invitrogen). MHC isoform analysis was performed as described (*18*). Briefly, MHC isoform composition was visualized using 8% acrylamide gels stained with Coomassie brilliant blue. MHC types I and IIB are well separated on gels, but the IIA overlaps with a small amount of IIX that exists in mouse skeletal muscle. Therefore, we refer to this band as IIA/X.

F-SL relation

Fiber bundles from skinned EDL, SOL, and DIA tissues were dissected for mechanics experiments (at least three fiber bundles per animal) and mounted using aluminum T clips between a length motor and a force transducer in an 802D Permeabilized Fiber Test Apparatus (Aurora Scientific Inc., Aurora, ON, Canada) on a Nikon Diaphot inverted microscope. SL was set using a high-speed VSL camera controlled by ASI 600A software (Aurora Scientific). Fiber bundles were maintained at 10°C, and the temperature was temporarily increased to 15°C during activation. Fibers were set in relaxing solution (pCa 8.5) then preactivated in relaxing solution with reduced 1 mM EGTA and activated in pCa 4.5 activating solution (40 mM BES, 10 mM $CaCO_3$-EGTA, 6.29 mM $MgCl_2$, 6.12 mM Na–adenosine triphosphate, 1 mM dithiothreitol, 45.3 mM K-propionate, 15 mM creatine phosphate, and protease inhibitors) at SL = 2.4 μm to record maximal active tension. The resting SL was readjusted to 2.4 μm after each activation-relaxation cycle. Specific force was expressed as force per cross-sectional area assuming elliptical fiber cross section. Most activations had internal SL shortening during force development and in some fiber bundles an initial shortening phase was followed by a slow stretch phase (most likely due to sarcomeres outside the field of view that were stronger and that continued to shorten) that was accompanied by a slow force creep. Force was recorded before the onset of the creep phase. To establish the descending limb, fiber bundles were sequentially activated at a range of SLs and SL was recorded both before and during activation. The passive F-SL curves were determined on the basis of the average of pre- and postactivation passive forces for each SL. Internal shortening correction was applied to passive forces during activation by using nonlinear standard curve interpolation. The passive force during activation was then subtracted from the maximal active force, isolating the active force generating potential for each fiber bundle at a given SL.

Super-resolution structured illumination microscopy

Skinned EDL, SOL, and DIA myofibril bundles were stretched from slack at different degrees (20 to 70%), fixed in 10% formalin, washed four times with PBS for 15 min, embedded in optimal cutting temperature (OCT) compound, and immediately frozen in 2-methylbutane precooled in liquid nitrogen. Four-micrometer-thick cryosections were then cut and mounted onto microscope slides. Tissue sections were permeabilized in 0.2% Triton X-100/PBS for 20 min at room temperature, blocked with 2% bovine serum albumin (BSA) and 1% normal donkey serum in PBS for 1 hour at 4°C, and incubated overnight at 4°C with primary antibodies diluted in blocking solution. The primary antibodies included: anti-nebulin N-terminal (no. 128, goat polyclonal; 1:250; Myomedix), anti-Tmod1 (1:375; X523-X524, rabbit polyclonal; no. 8627, BioGenes), anti-Tmod4 (1:375; X527-X528, rabbit polyclonal; no. 8629, BioGenes), anti-titin Ti102 [mouse monoclonal; 1:100; (*20*)], and anti–α-actinin (A7811, mouse monoclonal; 1:1000; Sigma-Aldrich). Sections were washed twice with PBS for 30 min and incubated with secondary antibodies diluted in PBS for 3 hours at room temperature. The secondary antibodies included: Alexa Fluor 405–conjugated donkey anti-mouse immunoglobulin G (IgG) H + L (1:100; ab175658, Abcam), Alexa Fluor 568–conjugated donkey anti-goat IgG H + L (1:500; A-11057, Invitrogen), and Alexa Fluor 647–conjugated donkey anti-rabbit IgG H + L (1:300; ab150063, Abcam). Thin filaments were visualized with Alexa Fluor 488–conjugated phalloidin (1:1000; A12379; Invitrogen) applied together with both the primary and the secondary antibodies. The sections were then washed twice with PBS for 15 min and covered with number 1.5H coverslips (Bioscience Tools, CSHP-No1.5-24x60) using ProLong Diamond (Thermo Fisher Scientific Inc.). A Zeiss ELYRA S1 SR-SIM microscope was used with ultraviolet light and solid-state laser (405/488/561/642 nm) illumination sources, oil immersion objectives 100× [numerical aperture (NA) = 1.46] and a 63× (NA = 1.4), and a scientific complementary metal-oxide semiconductor (sCMOS) camera. Typical imaging was performed on a 49.34 μm by 24.67 μm area with 1280 × 640 pixel dimensions. Typical image stacks composed of 40 slices were acquired with 0.084-μm Z-steps, five angles and five phases per angle for each slice. Image reconstruction and fluorescence intensity plot profile generation were performed with ZEN 2 software (Zeiss). Plot profiles of the antibody-labeled images were fit with Gaussian curves to determine the epitope peak position using Fityk 1.3.0 software. TFL was determined from the Tmod1/4 epitope positions across the Z-disk. Nebulin length was calculated from the N-terminal nebulin positions across the Z-disk. A-band width or length of the A-band titin was determined from the Ti102 epitope positions across the A-band. Plot profiles of phalloidin-stained images were fit with rectangular Gaussian functions. The height of the rectangular Gaussian function was normalized to the integral intensity of the phalloidin peak and set to 5% of the integral intensity. Phalloidin-based TFL was defined as the half width at half maximum of the rectangular Gaussians, and it showed good correlation with the Tmod1/4-based TFL measurements. The epitope distances were averaged in the SL range between 2.6 and 3.0 μm to allow comparison across the genotypes and different muscles with varying TFL. Epitope measurements in the compound-Het mice are less affected by the SL dependence because the two epitopes are directly comparable within a single sarcomere. Note that the N-terminal nebulin antibody was raised against a M1-M3 peptide, and its epitope can be anywhere in this sequence. In addition, there are 72 residues N-terminal from M1; based on structure predictions (56% α helix, 44% β strand), their maximal length when fully extended is ~17 nm (0.56 nm by 72 nm by 0.15 nm + 0.44 nm by 72 nm by 0.35 nm). Thus, the epitope labeled by the N-terminal antibody could be maximally 3 × 5.5 + 17 = 33.5 nm from nebulin's N terminus.

TEM and IEM

Skinned EDL from of ~8-week-old WT, $\mathrm{Neb}^{\Delta S9-11}$, $\mathrm{Neb}^{\mathrm{DupS9-11}}$, and $\mathrm{Neb}^{\Delta S9-11/\mathrm{DupS9-11}}$ compound-Het mice ($n = 4$) were stretched from the slack length at different degrees (~20 to 60%) and processed for TEM. Briefly, fixation of muscle tissue was performed with a mix of 3.7% paraformaldehyde, 3% glutaraldehyde, and 0.2% tannic acid in PBS (137 mM NaCl, 2.7 mM KCl, 10 mM Na_2HPO_4, and 1.8 mM KH_2PO_4) (pH 7.2) for 1 hour at 4°C. Then, muscles were postfixed in 1% OsO_4 in PBS for 30 min at 4°C. After this step, samples were dehydrated in an ethanol graded series, infiltrated with propylene oxide, and transferred to a mix of 1:1 propylene oxide:Araldite 502/Embed 812 (Epon-812, EMS). Subsequently, samples were transferred to a pure Araldite 502/Embed 812 resin and polymerized for 48 hours at 60°C. Ultrathin, 50-nm longitudinal sections were obtained with a Reichert-Jung ultramicrotome and contrasted with 1% potassium permanganate and lead citrate.

Observations used a TECNAI Spirit G2 TEM (FEI, Hillsboro, OR), and images were acquired with a side-mounted AMT Image Capture Engine V6.02 (4Mpix) digital camera operated at 100 kV. Digital images (1792 × 1792 pixels) were saved and calibrated for density plot profiles analysis with ImageJ 1.49v (NIH, USA) to obtain TFL measurements from the middle of the Z-disk to the H-zone (μm).

Ultrastructural immunolabeling of nebulin-N terminus was performed on skinned EDL from WT, $\mathrm{Neb}^{\Delta S9-11}$, $\mathrm{Neb}^{\mathrm{DupS9-11}}$, and $\mathrm{Neb}^{\Delta S9-11/\mathrm{DupS9-11}}$ mice ($n = 9$) stretched to different degrees from the slack length as before and processed by the pre-embedding technique previously described (*46*). Skeletal muscle specimens were skinned twice and washed in relaxing solution before fixation with 3.7% paraformaldehyde in PBS for 30 min at 4°C and then rinsed with PBS and with PBS containing protease inhibitors. Blocking was performed with 1% BSA in PBS containing protease inhibitors and 0.05% Tween 20, followed by the incubation with the anti-nebulin N terminus primary antibody from rabbit (0.2 mg/ml, 48 hours; Myomedix Ltd., Germany, no. 6969). After the rinsing step with PBS containing inhibitors, muscle fiber bundles were incubated with Nanogold (1.4 nm)-Fab' goat anti-rabbit antibody (80 μg/ml, 12 hours; no. 2004, Nanoprobes Inc., USA). All incubations were performed in a humidity chamber at 4°C. After labeling, muscle tissues were washed in PBS and fixed with 3% glutaraldehyde in the same buffer and then processed for TEM as before. Ultrathin sections of 90 nm were contrasted, and images were recorded and calibrated for analysis with ImageJ 1.49v (NIH, USA) as explained above. Density plot profiles of single sarcomeres were analyzed to determine the nebulin-N terminus epitope distance from the middle of the Z-disk. TFL was also measured in unlabeled sarcomeres from bundles of muscle fibers used as control experiments by substitution of the primary or secondary antibodies incubation with 1% BSA in PBS solution containing inhibitors. The TEM procedure is well known to cause shrinkage of the muscle structure. A shrinkage correction factor was calculated by the ratio of the in vivo thick filament length (A-bandwidth) 1.6 μm (*47*) and the measured A-bandwidth on our samples. This factor was then used to obtain the nebulin N terminus epitope distance and the TFL shrinkage-corrected values. Shrinkage was typically ~5%.

UDD surgery

Hundred-day-old male C57BL/6J mice ($n = 9$ UDD and $n = 7$ sham) and 58- to 70-day-old cLmod2 KO mice ($n = 10$ KO UDD and $n = 4$ WT UDD) were anaesthetized with 1 to 3% isoflurane, and a small incision was made in the neck area just above the clavicle. The phrenic nerve on the right side was isolated behind the sternohyoid muscle, and a 3- to 4-mm section was transected at the height of the supraclavicular nerve branch (*23*). Mice were closed up, allowed to recover, and were sacrificed 30 hours after denervation for tissue harvest.

Statistical analysis

Sample randomization and blinding of the investigator was applied in the case of the EM/IEM and SR-SIM image analysis where investigators were unaware of the genotype of the animals during the epitope distance measurement on the previously generated plot profiles. Whenever practical both male and female mice were used (no sex differences were found in any of our studies). Statistical analysis was performed using GraphPad Prism 6 (GraphPad Software Inc., La Jolla, CA). Descriptive statistical results are shown as means ± SD unless stated otherwise. Differences between groups were considered to be statistically significant at a probability value of $P < 0.05$. Two-tailed t test was used when comparing averages of two datasets. Welch's correction was applied in the case of unequal variances between the two groups. One-way ANOVA using Bonferroni post hoc analysis was performed to assess differences between multiple groups. To increase the statistical power of the tests equal or close to equal, sample size was applied within independent groups. Linear regression analysis was used to fit and compare the epitope distance data of the immunofluorescence- and IEM-based localization studies. Symbols used in statistical tests and on figures: ns, $P \geq 0.05$; $^{*}P < 0.05$; $^{**}P < 0.01$; $^{***}P < 0.001$; and $^{****}(^{\#\#\#\#})P < 0.0001$. Statistical details for each figure are provided in the caption with additional details in table S4.

SUPPLEMENTARY MATERIALS

Supplementary material for this article is available at http://advances.sciencemag.org/cgi/content/full/6/46/eabc1992/DC1

View/request a protocol for this paper from *Bio-protocol*.

REFERENCES AND NOTES

1. C. A. Ottenheijm, C. C. Witt, G. J. Stienen, S. Labeit, A. H. Beggs, H. Granzier, Thin filament length dysregulation contributes to muscle weakness in nemaline myopathy patients with nebulin deficiency. *Hum. Mol. Genet.* **18**, 2359–2369 (2009).
2. V. M. Fowler, R. Dominguez, Tropomodulins and leiomodins: Actin pointed end caps and nucleators in muscles. *Biophys. J.* **112**, 1742–1760 (2017).

3. R. C. Ahrens-Nicklas, C. T. Pappas, G. P. Farman, R. M. Mayfield, T. M. Larrinaga, L. Medne, A. Ritter, I. D. Krantz, C. Murali, K. Y. Lin, J. H. Berger, S. W. Yum, C. K. Carreon, C. C. Gregorio, Disruption of cardiac thin filament assembly arising from a mutation in LMOD2: A novel mechanism of neonatal dilated cardiomyopathy. *Sci. Adv.* **5**, eaax2066 (2019).
4. A. M. Gordon, E. Homsher, M. Regnier, Regulation of contraction in striated muscle. *Physiol. Rev.* **80**, 853–924 (2000).
5. J. P. Jin, K. Wang, Nebulin as a giant actin-binding template protein in skeletal muscle sarcomere. Interaction of actin and cloned human nebulin fragments. *FEBS Lett.* **281**, 93–96 (1991).
6. J. Wright, Q. Q. Huang, K. Wang, Nebulin is a full-length template of actin filaments in the skeletal muscle sarcomere: An immunoelectron microscopic study of its orientation and span with site-specific monoclonal antibodies. *J. Muscle Res. Cell Motil.* **14**, 476–483 (1993).
7. M. Kruger, J. Wright, K. Wang, Nebulin as a length regulator of thin filaments of vertebrate skeletal muscles: Correlation of thin filament length, nebulin size, and epitope profile. *J. Cell Biol.* **115**, 97–107 (1991).
8. S. Labeit, T. Gibson, A. Lakey, K. Leonard, M. Zeviani, P. Knight, J. Wardale, J. Trinick, Evidence that nebulin is a protein-ruler in muscle thin filaments. *FEBS Lett.* **282**, 313–316 (1991).
9. K. Wang, M. Knipfer, Q. Q. Huang, A. van Heerden, L. C. Hsu, G. Gutierrez, X. L. Quian, H. Stedman, Human skeletal muscle nebulin sequence encodes a blueprint for thin filament architecture. Sequence motifs and affinity profiles of tandem repeats and terminal SH3. *J. Biol. Chem.* **271**, 4304–4314 (1996).
10. C. T. Pappas, R. M. Mayfield, C. Henderson, N. Jamilpour, C. Cover, Z. Hernandez, K. R. Hutchinson, M. Chu, K. H. Nam, J. M. Valdez, P. K. Wong, H. L. Granzier, C. C. Gregorio, Knockout of Lmod2 results in shorter thin filaments followed by dilated cardiomyopathy and juvenile lethality. *Proc. Natl. Acad. Sci. U.S.A.* **112**, 13573–13578 (2015).
11. D. S. Gokhin, J. Ochala, A. A. Domenighetti, V. M. Fowler, Tropomodulin 1 directly controls thin filament length in both wild-type and tropomodulin 4-deficient skeletal muscle. *Development* **142**, 4351–4362 (2015).
12. C. T. Pappas, G. P. Farman, R. M. Mayfield, J. P. Konhilas, C. C. Gregorio, Cardiac-specific knockout of Lmod2 results in a severe reduction in myofilament force production and rapid cardiac failure. *J. Mol. Cell. Cardiol.* **122**, 88–97 (2018).
13. M. Yuen, S. A. Sandaradura, J. J. Dowling, A. S. Kostyukova, N. Moroz, K. G. Quinlan, V. L. Lehtokari, G. Ravenscroft, E. J. Todd, O. Ceyhan-Birsoy, D. S. Gokhin, J. Maluenda, M. Lek, F. Nolent, C. T. Pappas, S. M. Novak, A. D'Amico, E. Malfatti, B. P. Thomas, S. B. Gabriel, N. Gupta, M. J. Daly, B. Ilkovski, P. J. Houweling, A. E. Davidson, L. C. Swanson, C. A. Brownstein, V. A. Gupta, L. Medne, P. Shannon, N. Martin, D. P. Bick, A. Flisberg, E. Holmberg, P. Van den Bergh, P. Lapunzina, L. B. Waddell, D. D. Sloboda, E. Bertini, D. Chitayat, W. R. Telfer, A. Laquerriere, C. C. Gregorio, C. A. Ottenheijm, C. G. Bonnemann, K. Pelin, A. H. Beggs, Y. K. Hayashi, N. B. Romero, N. G. Laing, I. Nishino, C. Wallgren-Pettersson, J. Melki, V. M. Fowler, D. G. MacArthur, K. N. North, N. F. Clarke, Leiomodin-3 dysfunction results in thin filament disorganization and nemaline myopathy. *J. Clin. Invest.* **125**, 456–457 (2015).
14. D. S. Gokhin, V. M. Fowler, A two-segment model for thin filament architecture in skeletal muscle. *Nat. Rev. Mol. Cell Biol.* **14**, 113–119 (2013).
15. S. T. Kazmierski, P. B. Antin, C. C. Witt, N. Huebner, A. S. McElhinny, S. Labeit, C. C. Gregorio, The complete mouse nebulin gene sequence and the identification of cardiac nebulin. *J. Mol. Biol.* **328**, 835–846 (2003).
16. K. Donner, K. J. Nowak, M. Aro, K. Pelin, C. Wallgren-Pettersson, Developmental and muscle-type-specific expression of mouse nebulin exons 127 and 128. *Genomics* **88**, 489–495 (2006).
17. P. K. Luther, The vertebrate muscle Z-disc: Sarcomere anchor for structure and signalling. *J. Muscle Res. Cell Motil.* **30**, 171–185 (2009).
18. F. Li, D. Buck, J. De Winter, J. Kolb, H. Meng, C. Birch, R. Slater, Y. N. Escobar, J. E. Smith 3rd, L. Yang, J. Konhilas, M. W. Lawlor, C. Ottenheijm, H. L. Granzier, Nebulin deficiency in adult muscle causes sarcomere defects and muscle-type-dependent changes in trophicity: Novel insights in nemaline myopathy. *Hum. Mol. Genet.* **24**, 5219–5233 (2015).
19. F. Li, J. Kolb, J. Crudele, Z. Hourani, J. E. Smith 3rd, J. S. Chamberlain, H. Granzier, Expressing a Z-disk nebulin fragment in nebulin-deficient mouse muscle: Effects on muscle structure and function. *Skelet. Muscle* **10**, 2 (2020).
20. K. Trombitas, M. Greaser, S. Labeit, J. P. Jin, M. Kellermayer, M. Helmes, H. Granzier, Titin extensibility in situ: Entropic elasticity of permanently folded and permanently unfolded molecular segments. *J. Cell Biol.* **140**, 853–859 (1998).
21. J. Kolb, F. Li, M. Methawasin, M. Adler, Y. N. Escobar, J. Nedrud, C. T. Pappas, S. P. Harris, H. Granzier, Thin filament length in the cardiac sarcomere varies with sarcomere length but is independent of titin and nebulin. *J. Mol. Cell. Cardiol.* **97**, 286–294 (2016).
22. A. Brynnel, Y. Hernandez, B. Kiss, J. Lindqvist, M. Adler, J. Kolb, R. van der Pijl, J. Gohlke, J. Strom, J. Smith, C. Ottenheijm, H. L. Granzier, Downsizing the molecular spring of the giant protein titin reveals that skeletal muscle titin determines passive stiffness and drives longitudinal hypertrophy. *eLife* **7**, e40532 (2018).
23. R. van der Pijl, J. Strom, S. Conijn, J. Lindqvist, S. Labeit, H. Granzier, C. Ottenheijm, Titin-based mechanosensing modulates muscle hypertrophy. *J. Cachexia. Sarcopenia Muscle* **9**, 947–961 (2018).
24. L. Mi-Mi, G. P. Farman, R. M. Mayfield, J. Strom, M. Chu, C. T. Pappas, C. C. Gregorio, In vivo elongation of thin filaments results in heart failure. *PLOS ONE* **15**, e0226138 (2020).
25. C. A. Ottenheijm, D. Buck, J. M. de Winter, C. Ferrara, N. Piroddi, C. Tesi, J. R. Jasper, F. I. Malik, H. Meng, G. J. Stienen, A. H. Beggs, S. Labeit, C. Poggesi, M. W. Lawlor, H. Granzier, Deleting exon 55 from the nebulin gene induces severe muscle weakness in a mouse model for nemaline myopathy. *Brain J. Neurol.* **136**, 1718–1731 (2013).
26. V. L. Lehtokari, R. S. Greenleaf, E. T. DeChene, M. Kellinsalmi, K. Pelin, N. G. Laing, A. H. Beggs, C. Wallgren-Pettersson, The exon 55 deletion in the nebulin gene--one single founder mutation with world-wide occurrence. *Neuromuscul. Disord.* **19**, 179–181 (2009).
27. K. Wang, J. Wright, Architecture of the sarcomere matrix of skeletal muscle: Immunoelectron microscopic evidence that suggests a set of parallel inextensible nebulin filaments anchored at the Z line. *J. Cell Biol.* **107**, 2199–2212 (1988).
28. D. S. Gokhin, E. A. Dubuc, K. Q. Lian, L. L. Peters, V. M. Fowler, Alterations in thin filament length during postnatal skeletal muscle development and aging in mice. *Front. Physiol.* **5**, 375 (2014).
29. D. S. Gokhin, R. A. Lewis, C. R. McKeown, R. B. Nowak, N. E. Kim, R. S. Littlefield, R. L. Lieber, V. M. Fowler, Tropomodulin isoforms regulate thin filament pointed-end capping and skeletal muscle physiology. *J. Cell Biol.* **189**, 95–109 (2010).
30. S. Millevoi, K. Trombitas, B. Kolmerer, S. Kostin, J. Schaper, K. Pelin, H. Granzier, S. Labeit, Characterization of nebulette and nebulin and emerging concepts of their roles for vertebrate Z-discs. *J. Mol. Biol.* **282**, 111–123 (1998).
31. C. T. Pappas, N. Bhattacharya, J. A. Cooper, C. C. Gregorio, Nebulin interacts with CapZ and regulates thin filament architecture within the Z-disc. *Mol. Biol. Cell* **19**, 1837–1847 (2008).
32. C. T. Pappas, P. A. Krieg, C. C. Gregorio, Nebulin regulates actin filament lengths by a stabilization mechanism. *J. Cell Biol.* **189**, 859–870 (2010).
33. M. Marttila, M. Hanif, E. Lemola, K. J. Nowak, J. Laitila, M. Gronholm, C. Wallgren-Pettersson, K. Pelin, Nebulin interactions with actin and tropomyosin are altered by disease-causing mutations. *Skelet. Muscle* **4**, 15 (2014).
34. A. Castillo, R. Nowak, K. P. Littlefield, V. M. Fowler, R. S. Littlefield, A nebulin ruler does not dictate thin filament lengths. *Biophys. J.* **96**, 1856–1865 (2009).
35. R. S. Littlefield, V. M. Fowler, Thin filament length regulation in striated muscle sarcomeres: Pointed-end dynamics go beyond a nebulin ruler. *Semin. Cell Dev. Biol.* **19**, 511–519 (2008).
36. T. Tsukada, C. T. Pappas, N. Moroz, P. B. Antin, A. S. Kostyukova, C. C. Gregorio, Leiomodin-2 is an antagonist of tropomodulin-1 at the pointed end of the thin filaments in cardiac muscle. *J. Cell Sci.* **123**, 3136–3145 (2010).
37. D. Szatmari, B. Bugyi, Z. Ujfalusi, L. Grama, R. Dudas, M. Nyitrai, Cardiac leiomodin2 binds to the sides of actin filaments and regulates the ATPase activity of myosin. *PLOS ONE* **12**, e0186288 (2017).
38. F. Li, E. R. Barton, H. Granzier, Deleting nebulin's C-terminus reveals its importance to sarcomeric structure and function and is sufficient to invoke nemaline myopathy. *Hum. Mol. Genet.* **28**, 1709–1725 (2019).
39. M. L. Bang, X. Li, R. Littlefield, S. Bremner, A. Thor, K. U. Knowlton, R. L. Lieber, J. Chen, Nebulin-deficient mice exhibit shorter thin filament lengths and reduced contractile function in skeletal muscle. *J. Cell Biol.* **173**, 905–916 (2006).
40. H. L. Granzier, H. A. Akster, H. E. Ter Keurs, Effect of thin filament length on the force-sarcomere length relation of skeletal muscle. *Am. J. Phys.* **260**, C1060–C1070 (1991).
41. A. Dobin, C. A. Davis, F. Schlesinger, J. Drenkow, C. Zaleski, S. Jha, P. Batut, M. Chaisson, T. R. Gingeras, STAR: Ultrafast universal RNA-seq aligner. *Bioinformatics* **29**, 15–21 (2013).
42. M. I. Love, W. Huber, S. Anders, Moderated estimation of fold change and dispersion for RNA-seq data with DESeq2. *Genome Biol.* **15**, 550 (2014).
43. E. Mancini, J. Iserte, M. C. A Yanovsky, ASpli: Analysis of alternative splicing using RNA-Seq. R package version 1.12.0. (2019).
44. C. Hidalgo, B. Hudson, J. Bogomolovas, Y. Zhu, B. Anderson, M. Greaser, S. Labeit, H. Granzier, PKC phosphorylation of titin's PEVK element: A novel and conserved pathway for modulating myocardial stiffness. *Circ. Res.* **105**, 631–638 (2009).
45. D. Buck, B. D. Hudson, C. A. Ottenheijm, S. Labeit, H. Granzier, Differential splicing of the large sarcomeric protein nebulin during skeletal muscle development. *J. Struct. Biol.* **170**, 325–333 (2010).
46. P. Tonino, B. Kiss, J. Strom, M. Methawasin, J. E. Smith 3rd, J. Kolb, S. Labeit, H. Granzier, The giant protein titin regulates the length of the striated muscle thick filament. *Nat. Commun.* **8**, 1041 (2017).
47. H. Sosa, D. Popp, G. Ouyang, H. E. Huxley, Ultrastructure of skeletal muscle fibers studied by a plunge quick freezing method: Myofilament lengths. *Biophys. J.* **67**, 283–292 (1994).

Acknowledgments: We are grateful to laboratory members (in particular, X. Liu, X. Zhou, C. Saripalli, O. Brynnel, M. Adler, J. Simon, R. Mayfield, and C. Pappas), the University of Arizona

Genetic Engineering of Mouse Models (GEMM) Core, the Mouse Phenotyping Core, the Viral Production Core, and the Imaging Core facilities. **Funding:** This work was supported by grants from A Foundation Building Strength (H.G.), National Heart lung and Blood Institute RO1 HL123078 (C.G.), and National Institute of Arthritis and Musculoskeletal and Skin Disease grant R01 AR053897 (H.G.). **Author contributions:** B.K., J.K., J.E.S., and H.G. designed the study. B.K., J.G., J.S., J.K., J.E.S., and Z.H. collected the data. B.K., J.G., J.S., J.K., J.E.S., Z.H., and H.G. analyzed the data. B.K., J.K., J.E.S., HG, C.G., C.O., and H.G. interpreted the data and wrote the manuscripts. All authors revised, reviewed, and approved of the final version of the manuscript. **Competing interests:** The authors declare that they have no competing interests. **Data and materials availability:** The raw RNA-seq data that support the findings of this study are available under BioProject accession number PRJNA613762. All additional unique materials (protocols, animal models, etc.) and all data that support the findings of this study are available from the corresponding author upon reasonable request.

Submitted 11 April 2020
Accepted 23 September 2020
Published 11 November 2020
10.1126/sciadv.abc1992

Citation: B. Kiss, J. Gohlke, P. Tonino, Z. Hourani, J. Kolb, J. Strom, O. Alekhina, J. E. Smith III, C. Ottenheijm, C. Gregorio, H. Granzier, Nebulin and Lmod2 are critical for specifying thin-filament length in skeletal muscle. *Sci. Adv.* **6**, eabc1992 (2020).